Simulations of Long-Column Flow Experiments Related to Geologic Carbon Sequestration: Effects of Outer Wall Boundary Condition on Upward Flow and Formation of Liquid CO_2

C.M. Oldenburg, C. Doughty, C.A. Peters, and P.F. Dobson

Earth Sciences Division 74-316C
Lawrence Berkeley National Laboratory
Berkeley, CA 94720

Department of Civil and Environmental Engineering
Princeton University
Princeton, NJ 08544

Abstract

Improving understanding of CO_2 migration, phase change, and trapping processes motivates development of large-scale laboratory experiments to bridge the gap between bench-scale experiments and field-scale studies. Critical to the design of such experiments are defensible configurations that mimic relevant subsurface flow scenarios. We use numerical simulation with TOUGH2/ECO2M and ECO2N to design flow and transport experiments aimed at understanding upward flows including the transition of CO_2 from super-critical to liquid and gaseous forms. These experiments are designed for a large-scale facility such as the proposed "Laboratory for Underground CO_2 Investigations" (LUCI). LUCI would consist of one or more long-column pressure vessels (LCPVs) several hundred meters in length filled with porous materials. An LCPV with an insulated outer wall corresponds to the column being at the center of a large upwelling plume. If the outer wall of the LCPV is assigned fixed temperature boundary conditions corresponding to the geothermal gradient, the LCPV represents a narrow upwelling through a fault or well. Numerical simulations of upward flow in the columns reveal complex temporal variations of temperature and saturation, including the appearance of liquid CO_2 due to expansion cooling. The results are sensitive to outer thermal boundary conditions. Understanding of the simulations is aided by time-series animations of saturation-depth profiles and trajectories through *P-T* (pressure-temperature) space with superimposed phase saturations. The strong dependence of flow on hydrologic properties and the lack of knowledge of three-phase relative permeability and hysteresis underlines the need for large-scale flow experiments to understand multiphase leakage behavior.

Introduction

In the context of geologic carbon sequestration (GCS), concerns about CO_2 leakage and associated environmental impacts and liabilities motivate research to elucidate and quantify processes governing upward flow and transport of CO_2. With only a handful of demonstration and industrial projects available, a large amount of research into the performance of GCS is carried out by numerical simulation. Beyond the well-accepted process models such as Darcy's Law for fluid flow, Fick's Law for molecular diffusion, and Fourier's Law for conductive heat transfer, there are numerous multiphase, multicomponent, and process couplings that are not as well understood and whose prediction depends to a large degree on empiricism, essentially upscaled laboratory measurements and experiments. Progress in the understanding of GCS processes therefore requires encoding into simulators defensible physical and chemical process models often developed through laboratory experimentation.

One limitation of laboratory experiments is the length scale, which is generally restricted to bench scale with a maximum length on the order of one meter. This limitation restricts the aspects of GCS that can be tested in the laboratory and in particular is inconsistent with the practice of GCS which is by nature a very large-scale process. For example, upward CO_2 migration and associated depressurization through unexpected leakage pathways will be accompanied by a large expansion as CO_2 transitions from the supercritical or liquid conditions of the storage formation to gaseous conditions at shallower depths[1]. In order to study and understand such processes and related changes in flow velocity, temperature (e.g., by expansion cooling), and trapping in the porous medium, ideally one needs to run experiments over long vertical length scales to encompass a sufficiently large hydrostatic pressure difference that naturally spans the critical pressure.

The need for long vertical columns presents an enormous practical challenge. At least one experiment focusing on CO_2 dissolution has been carried out in a long tube suspended in the stairwell of a tall building[2]. Slim-tube approaches used in the oil and gas industry (e.g., Carlson[3]; Maloney and Briceno[4]) provide another method of representing a long flow path, but because slim-tubes are normally deployed as tight coils, e.g., for convenience in placing them within ovens for temperature control, they do not provide a hydrostatic pressure gradient. Underground laboratories provide another opportunity for developing pressure-controlled long vertical flow columns, an approach our team has conceptualized for the "Laboratory for Underground CO_2 Investigations" (LUCI)[5].

As proponents of large-scale experiments, it is incumbent upon us to clarify what experiments need to be done and what the experiments represent. The experiments we are considering are focused on understanding upward flow of CO_2 and brine and the processes related to decompression expansion of CO_2 including cooling and residual phase trapping. Examples of some of the questions that can be addressed through experiments in the facility and that are considered in this study include the following:

- Will upward flow of CO_2 accelerate as it decompresses through the critical pressure?
- What is the extent of cooling due to decompression expansion?
- In addition to the supercritical to gas transition, can liquid CO_2 form?
- How much CO_2 becomes trapped by residual phase trapping during upward flow of CO_2?

The long-column pressure vessels (LCPVs) filled with sand and brine that we are proposing for LUCI will be designed to represent 500 m vertical sections of the subsurface over a depth range controllable by specification of bottom and top pressure and temperature conditions. As an effectively one-dimensional system, the LCPV would formally represent either an actual one-dimensional flow path such as a leaky well (e.g., Gasda et al.[6]), or a small region in the middle of a vast upward-rising plume. We can control which of these scenarios we want to test through the application of different thermal boundary conditions on the outer wall of the LCPV. With an understanding developed from numerical simulations of how flow might occur in the LCPV system, precise specifications of the system can be made and used to design and build the facility.

The purpose of this paper is to present simulations of experiments that could be carried out in a specific LCPV and to demonstrate the sensitivity of the formation of liquid CO_2 to the choice of boundary conditions and CO_2 release configurations. We emphasize that this paper is not about modeling upward CO_2 and brine flow in natural systems, but rather on simulating flow and transport in a potential future LCPV experimental apparatus designed to represent natural systems. As such, the parameters and properties of the system are chosen to be those of the engineered LCPV system, not those of any natural system. Although this work was carried out as part of our design calculations for LUCI which is focused on understanding leakage of CO_2 from deep geologic storage formations, the results are relevant to the broader modeling and experimentation community interested in conceptual models, choice of boundary conditions, models and parameters related to three-phase relative permeability, and numerical simulation of multiphase flows in general.

Background

Despite the well-recognized urgency to address global CO_2 emissions to mitigate anthropogenic climate change, relatively little progress has been made in implementing large-scale Carbon Dioxide Capture and Storage (CCS) world-wide. The main reason is the high cost of the activity in terms of dollars and energy penalty (e.g., House et al.[7]). Another reason for hesitation in large-scale implementation of CCS is the ongoing concern for subsurface impacts and hazards of injecting millions of tonnes of CO_2 annually. To address these concerns, researchers have been using all of the approaches available to understand the various possible consequences of CO_2 injection. The one feature of CCS that makes it stand out is the large scale of the process

through the entire chain from capture, to transportation, to storage. The vast amounts of CO_2 that will be injected and the large length scales and long time scales associated with some of the relevant processes make traditional laboratory experiments of limited value. What is needed to complement traditional laboratory experiments are medium and large-scale well-controlled, systematically monitored flow and transport experiments.

With the goal of establishing a large-scale flow and transport test facility, we have been working on the siting and design of LUCI[5]. Our initial venue for the facility was DUSEL (Deep Underground Science and Engineering Laboratory) located in the old Homestake Mine in Lead, South Dakota[8]. At DUSEL, we designed the facility to have a single shaft of diameter 3 m (a so-called raise-bore) with a height of approximately 500 m. Within the raise-bore there would be three LCPVs made of carbon steel of diameter approximately 1 m suspended from the top. Each of the LCPVs would have an inner access well for wire-line deployment of monitoring instruments. The annular space in the LCPV would be filled with porous materials of whatever properties were of interest for the given experiment.

Compressors, pumps, tanks, fluid reservoirs, flow controllers, and safety equipment would be deployed at the top and bottom ends of the raise-bore. The top of the raise-bore was planned to terminate in a building at the ground surface where wire-line hoists and overhead lifting capabilities could be used to deploy the monitoring equipment in the access wells of each LCPV. Intermediate sampling ports would be constructed throughout the length of the LCPVs within the raise-bore facilitated by existing horizontal drifts within the DUSEL facility. Thermal control treatments (insulation, heat tape, fluid tubing) would surround each LCPV independently throughout their lengths in the raise-bore. An Alimak™ raise-bore climber was considered to allow human access to the entire length of the raise-bore. The collection of the three LCPVs would then be available as a facility for independent closely controlled flow and transport experiments over unprecedented length scales. The 500 m length was chosen such that the transition of CO_2 from supercritical or liquid conditions to gaseous conditions could be easily captured through the natural gravitational pressure increase in the columns. For example, by holding the pressure at the top of an LCPV at 3.5 MPa, the hydrostatic pressure at the bottom of a brine-filled LCPV would be approximately 9 MPa, putting the critical pressure of 7.4 MPa 150 m from the bottom.

A facility like LUCI could be sited at any place where there is sufficient vertical relief, such as in a tall building or on the side of a high cliff. The mine environment provides several advantages including opportunities for ground support of the LCPVs, stable environmental conditions, ease of access, and a measure of containment if there were to be an accidental release from a pressurized vessel. We emphasize that CO_2 at LUCI would be confined to the LCPVs and not released to the environment.

Approach

Conceptual Models

In general, large-scale upward flow of CO_2 injected for GCS will tend to occur due to buoyancy effects. Conceptual models are shown in Figure 1 of the two broad classes of possible upward migration of CO_2 being considered here, specifically, an abandoned well and a leaky fault. In the case of the abandoned well, upward flow could be approximated as one-dimensional over long vertical length scales regardless of the specific flow paths within the well. For the leaky fault, the scenario shown in Figure 1 represents a leak from the storage region that develops into a large upwelling of CO_2 that could occur within a thick relatively uniform hydrologic system. The gray bar depicts a hypothetical one-dimensional geometry that would approximate flow near the center of such a large upwelling. Within these two broad classes of upward flows there are two distinct scenarios: (1) the case in which the flow is pseudo-steady with CO_2 constantly supplied from below; and (2) the case in which the CO_2 is supplied episodically or in one pulse creating an upward-rising bubble of CO_2. In this study, we consider both scenarios, by modeling either a constant supply of CO_2 from the bottom, or a rising bubble detached from any source. Assuming effectively one-dimensional flows occur in the well and fault leakage scenario, there arises the question of what conditions one should implement on the outer boundaries of the LCPVs to represent the particular flow scenario of interest. The simulations we present below will show the effects on the flow system of the choice of thermal boundary conditions on the outer wall. Because heat transfer to the rising CO_2 occurs between the solid grains, the liquid in the pores, and the outer wall boundary (depending on the scenario), we refer to the cooling that occurs as CO_2 rises upward as expansion cooling rather than Joule-Thomson cooling which, strictly speaking, would only occur in an isenthalpic system.

Boundary Conditions

For the case of the LCPV representing a large upwelling of CO_2, an insulated thermal boundary condition is appropriate for the outer side of the annular LCPV. This choice is justified by the large mass of upwelling CO_2 in which the edge of the plume is very far away. In this scenario, horizontal heat transfer would be minimal because of the relatively one-dimensional nature of the flow problem near the center of the upwelling plume and lack of thermal gradients in the lateral direction. On the other hand, modeling CO_2 flowing up a narrow conduit at a low flow rate would require a constant geothermal-gradient boundary condition to represent the large thermal inertia of the surroundings and the minimal heat supplied by the relatively small flow volume in the conduit. Either thermal boundary condition can be implemented in the experimental facility by appropriate treatment of the outer wall of the steel LCPV. The question that we address here is how sensitive the flow in the column will be to the choice of thermal boundary conditions.

A sketch of the long-column pressure vessel with large horizontal exaggeration is shown in Figure 2 along with the radially symmetric domain used for the simulations. The left-hand side

(LHS) boundary is placed at the wall of the inner access well which will be used for monitoring the annular flow region using various down-hole geophysical monitoring tools. This access well is currently specified to be made out of fiberglass and filled with brine under hydrostatic conditions to avoid large pressure gradients that could burst the inner wall. We assume a closed boundary (no-flow and insulated) for the inner-wall (LHS) for all of the simulations presented here. The bottom of the LCPV is also closed and insulated but includes flow ports such that CO_2 can be injected at a controlled rate into the bottom of the LCPV. The top of the column is held at constant *P-T* conditions of 3.43 MPa and 23.75 °C. These conditions correspond roughly to a depth of about 350 m in a typical sedimentary basin. Under these conditions and with NaCl brine of 100,000 ppm concentration, the *P-T* at the bottom of the 500 m-long LCPV are 8.67 MPa and 36.25 °C. We note finally that under these conditions, the critical pressure and temperature for CO_2 are located at approximately -380 m and -295 m as measured downward within the LCPV, respectively.

The boundary conditions are summarized in Table 1. We implement these boundary conditions through standard techniques in the TOUGH2 framework. Specifically, a fixed geothermal gradient boundary condition is implemented by setting the thermal heat energy contained in the gridblocks at the boundary to an effectively infinite value (by setting either gridblock volume, rock heat capacity, or rock density to a very large value) so that, regardless of how much heat flows into or out of the gridblock, its temperature remains the same. These fixed-temperature gridblocks are made closed to flow by setting their permeability to zero and using harmonic weighting of permeability at interfaces between gridblocks. The open boundary conditions are implemented by giving the boundary gridblocks non-zero permeability and effectively infinite volume such that their pressures and temperatures remain constant regardless of how much fluid and heat flows in or out. The closed-to-flow and thermally insulated boundary conditions are implemented simply by using finite-volume gridblocks with normal flow and thermal properties at the boundaries of the domain.

Flow System Properties

The model LCPV flow domain is assumed to be filled with unconsolidated sand such as one would emplace by slurry or tremie methods in the actual LCPV. The homogeneous coarse sand was chosen to allow fluid flow in the column over practical experimental time scales rather than to represent any particular sedimentary basin or reservoir system. Specific properties of the unconsolidated sand were estimated using the Rosetta Database[9] which resulted in porosity, permeability, and capillary and relative permeability parameters shown in Table 2. For cases in which liquid- and gas-phase CO_2 co-exist along with aqueous-phase brine, the three-phase capillary pressure and relative permeability formulations of Parker et al. (1987)[11] are used. The values of capillary pressure for supercritical, gaseous, and liquid CO_2 for a given aqueous-phase saturation are assumed to be the same (i.e., we assume no interfacial tension between the various phases of CO_2). The porous sand is assumed to be unreactive and immobile during all flow processes, i.e., reactive geochemistry and geomechanical stresses and deformation are neglected.

We also neglect molecular diffusion because we have observed in test simulations not presented here its negligible effect in this high-permeability system.

Hysteretic capillary pressure and relative permeability functions are needed when drainage (drying) and imbibition (wetting) occur simultaneously in different parts of the flow domain, such as happens in the rising-bubble case. For this case, we use the hysteretic formulation described in Doughty[12], Niemi and Bodvarsson[13], and Finsterle et al.[14], in which capillary pressure is based on the van Genuchten[15] function, residual gas saturation for imbibition is calculated using the Land[16] equation, and interpolation between drainage and imbibition branches is done using the dependent domain theory of Mualem[17]. Hysteretic relative permeability functions are taken from Parker and Lenhard[18] and Lenhard and Parker[19]. In all discussions of the hysteretic functions, we use "gas" to refer to the non-wetting CO_2-rich phase, whether it is gaseous or supercritical. The hysteretic functions are illustrated in Figure 3 for the parameters given in Table 2. With this choice of parameters, the drainage branches of the capillary pressure and relative permeability functions for the rising-bubble case are identical to the capillary pressure and relative permeability functions for the two-phase domains of the constant-injection case. Hysteretic functions were not specified for the constant-injection case because the system was expected to always remain on the drainage branch, i.e., CO_2 is injected constantly, resulting in a monotonic drying processes. It turns out that small oscillations in CO_2 saturation do occur (see results section below), but saturation decreases are so small that using a non-hysteretic treatment is justified. The fact that the constant-injection case is essentially monotonically drying is convenient, because we are not aware of the existence of a three-phase hysteretic model for CO_2-water systems.

Figure 2 shows that the RHS (outer wall) boundary includes the actual 5 cm-thick carbon steel wall with properties as shown in Table 2. This wall is assumed to be in contact with the outer-wall boundary condition for the fixed geothermal gradient case. Despite the fact that this wall conducts heat rapidly, we model conduction through the wall for the fixed geothermal gradient boundary condition cases to be sure we capture whatever influence the steel wall may provide. Note for the insulated boundary condition cases, we assume the wall is in thermal equilibrium with the fluid in the flow domain and do not model conduction in the steel wall.

For injection into the domain at the bottom, we assume a constant injection rate distributed in the radial direction to produce a uniform mass flux over the bottom boundary. The total mass injection rate at the bottom of the LCPV is 1.58×10^{-2} kg/s (1.36 tonnes/d). This flow rate was derived by augmenting by a factor of two results from preliminary simulations that implemented a constant hydrostatic pressure bottom boundary with CO_2 saturation at the boundary equal to one so that only pure CO_2 phase would enter the brine-saturated column by buoyancy effects. We augmented the injection rate above the pure buoyant equivalent rate to make a flow system that would evolve on a relatively short time scale convenient for the experimentalists who would

be operating LUCI. The CO_2 injected at the bottom is into a row of gridblocks with infinite heat capacity which implements a constant-temperature injection.

The top constant-pressure boundary of the rising-bubble case requires special consideration because once the CO_2 bubble rises up and out of the top boundary, there is potential for fluid to flow back into the system through the top and we must specify the properties of this inflowing fluid. In our modeling, we have assumed that brine of the same temperature as the top boundary is available to flow back into the system if conditions dictate such flow. This boundary condition could be realized in the actual LUCI facility through the use of a pressurized brine reservoir into which CO_2 would enter and bubble upwards leaving brine at the bottom available for return to the top of the column.

Simulation

We carried out numerical simulations of CO_2 and brine flow in the LCPVs using TOUGH2 [20, 21] and the equation of state modules ECO2N[22, 23] and ECO2M [24, 25], a new member of the TOUGH2 family of codes. Briefly, TOUGH2 solves the transient integral finite difference multicomponent mass conservation equations and thermal energy equation along with the multiphase version of Darcy's Law for flow through porous media with implicit time stepping. The linear equations describing the changes in primary variables at each time step are solved using sparse-matrix conjugate gradient solvers, while non-linearity is handled using Newton's Method. TOUGH2 uses adaptive time-stepping and a residual-based convergence criterion at each time step that is very good at handling strong non-linearities and avoiding false convergence. The discretization used for the simulations is shown in Figure 4.

ECO2N and ECO2M are equation of state modules that describe the pure-component and mixture properties of water, NaCl, and CO_2. Whereas ECO2N can model CO_2 transitioning from gaseous to supercritical conditions, and from supercritical to liquid conditions, it cannot describe the phase change of CO_2 from gas to liquid conditions[23]. ECO2M, on the other hand, can model the full range of phase conditions in the system H_2O-NaCl-CO_2 including *P-T* conditions on the liquid-gas phase boundary (saturation line) with potential for three-phase conditions (aqueous, liquid CO_2, and gaseous CO_2). Because of its complete description of possible phase conditions, ECO2M is capable of simulating any scenario of upward CO_2 and brine flow including the formation of liquid CO_2. Our choice to use either ECO2M or ECO2N for the various cases studied here was based on whether the system modeled would involve gas-liquid phase change.

Some authors have pointed out the importance of considering the change in gravitational potential in the calculation of the enthalpy of rising fluids[26, 27. 28]. Comparison of the enthalpy change due to pressure change in the system from top to bottom with the gravitational potential change reveals the change in gravitational potential over 500 m is insignificant relative to the pressure-volume term for the CO_2 rise scenario considered here. Therefore, we have neglected the gravitational potential in the energy balance equations.

Results

Visualization

Because of the complex dynamics of the LCPV flow system in terms of the evolution of temperature and the various phases of CO_2, we present simulation results in a variety of different ways. We begin with traditional contour plots of pressure P, temperature T, CO_2 saturation S_{CO2}, and CO_2 density ρ_{CO2} in the 2D radial domain to show lateral variations and to provide a foundation for the more abstract but information-rich presentation of one-dimensional profiles in P-T space. The S_{CO2} variable is the sum of gaseous, liquid, and supercritical CO_2, and ρ_{CO2} is the saturation-weighted sum of gaseous, liquid, and supercritical densities. Trajectories over time in P-T space with saturation information at specific points show how the system changes as the CO_2 front passes by. Vertical profiles of pressure and temperature in P-T space show the phase evolution of fluid in the column and the tendency to migrate toward and then stay on the liquid-gas phase boundary when expansion cooling is significant.

Fixed geothermal gradient boundary, constant injection

In this scenario, CO_2 is injected at a constant rate and temperature into the bottom of the LCPV which is initially filled with NaCl brine at 100,000 ppm concentration at hydrostatic pressure and temperature equal to the geothermal gradient. Temperature at the outer wall or RHS boundary is held fixed at this geothermal gradient profile so that it is unchanged with time. We use TOUGH2/ECO2M for this simulation. This initial condition is shown in Figure 5 through contour plots of P and T (S_{CO2}, and ρ_{CO2} are zero at t = 0 because CO_2 injection has not started).

Figure 6 shows results at t = 5 d following the start of injection. As shown, the CO_2 front has moved upwards approximately 260 m creating a region of two-phase gaseous and super-critical CO_2 ($scCO_2$)-brine mixture. The pressure in the system increases due to this injection process. Isotherms are generally lifted upwards as the brine is displaced upwards and the injected CO_2 is at the relatively warmer temperature of the bottom boundary. The injected CO_2 decompresses as it rises upward through the hydrostatic pressure of the brine column and may exchange heat with the outer wall of the column. This is different from the scenario of CO_2 injection into a low-pressure gas-filled region, which involves strong decompression and accompanying expansion cooling only near the injection point[29]. Note in the figures the pressure gradient apparent near the RHS boundary formed by the difference in pressure between the flow domain and the boundary condition does not produce any flow because the steel wall has zero permeability. Overall, the simulation shows some minor two-dimensional effects arising from the fixed geothermal gradient boundary condition on the outer wall (RHS).

Figure 7 shows results at t = 10 d following the start of injection. The CO_2 front has now broken through to the top and the two-phase region of CO_2 and brine extends the full length of the column with associated drop in pressure. Comparison of the pressure and temperature plots shows that the fluid flow is essentially one-dimensional, while the temperature field shows two-

dimensional heat flow imparted by the fixed geothermal gradient RHS boundary. As shown by the temperature plot, expansion cooling occurs throughout the length of the column and especially along the inner wall (LHS) where the heating effects of the fixed temperature RHS boundary condition are weaker. The initial pressure rise and subsequent pressure drop as breakthrough occurs make the expansion cooling slightly larger than it would have been if the system had been held at hydrostatic pressure from the beginning.

The nearly one-dimensional nature of the flow problem allows us to plot results as vertical profiles through the system. Figure 8 shows values of P, T, S_{CO2}, and ρ_{CO2} for vertical profiles along the LHS of the LCPV at four times to explicitly show the vertical variations in temperature and phase conditions in the system, for example, the clear indication of the phase front. Note also that we include the liquid-gas phase boundary in the temperature plot. This curve represents the locus of points along which gas and liquid CO_2 are in equilibrium at the given pressure of the system. At t = 5 d, the CO_2 is supercritical below approximately -320 m and gaseous above. The effects of expansion cooling at t = 5 d can be seen clearly on the vertical profile plots of Figure 8a by the deflection toward lower temperatures at around z = -350 m and near-intersection with the liquid-gas phase boundary.

We present in Figure 9 a summary of the transient evolution of the behavior of the system in P-T space at five different points in the domain (z = -100 m, -200 m, -300 m, -400 m, and -500 m). Figure 9 shows the trajectory in P-T space of the system at each of these points along with S_{CO2} indicated by the color of the curve. As shown, at the deepest location (z = -500 m) just above the boundary where CO_2 injection occurs, the system pressurizes quickly and then heats during injection, after which it cools and depressurizes after breakthrough of the CO_2 out of the top of the system following a nearly reversible path. At z = -400 m, the path is more interesting in that expansion cooling is evident as CO_2 passes by. After 20 days, the outer-wall boundary exerts its influence on temperature and the point heats up again to nearly its initial temperature. At z = -300 m, following the common pressurization and heating that occurs upon startup of injection, expansion cooling is very evident and the system migrates close to the critical point, after which time it stays just below the liquid-gas phase boundary (in gaseous conditions) before further depressurizing as CO_2 breakthrough occurs at the top of the LCPV. At z = -200 m and -100 m, the behavior in P-T space is somewhat less dramatic because there is no significant expansion cooling at these shallow depths, and the cycle of rising and falling P and T is dominated by the passing of the injected CO_2 front and its breakthrough out the top of the column.

In Figure 10, we show results of the same simulation by plotting saturations on a vertical profile along the LHS of the system in P-T space at four different times. Animations of this figure available in Supplementary Material are particularly useful for visualizing how the system evolves. For this case of a constant geothermal gradient RHS boundary, thermal conduction from the outer wall is sufficient to keep the system out of the liquid-stable region despite the expansion cooling effects.

Insulated boundary, constant injection

To understand the effect of the outer wall (RHS) thermal boundary condition, we consider next a case identical to the above except the RHS (outer wall) is perfectly insulated. Results from TOUGH2/ECO2M at t = 5 d are shown in Figure 11 for comparison to Figure 6. The first observation is that the system behaves essentially like a one-dimensional system in terms of fluid (P) and heat (T) flow with no lateral variation whatsoever. Second, we see that with no heat entering or leaving through the RHS boundary, the intrinsic thermal effects are more obvious as they are controlled solely by advection, conduction, expansion, and phase change effects with no influence by radial heat conduction.

Vertical profiles of results for t = 5 d, 10 d, 20 d, and 30 d are shown in Figure 12. As shown, interesting oscillations in temperature occur at various times resulting in liquid CO_2 conditions alternating with $scCO_2$ and gaseous CO_2. The occurrence of liquid CO_2 causes phase interference that impedes upward flow and introduces a negative feedback to the expected expansion cooling, resulting in oscillations in density and temperature. At t = 30 d, liquid CO_2 is present from z = -200 m to -370 m. The existence of a large region of liquid CO_2 points to the importance of expansion cooling in large-scale buoyant CO_2 rise, at least for systems with high porosity and permeability. This cooling is further indicated in Figure 13 by the temporal evolution in P-T space at five different locations in the system. As shown for locations z = -300 m and -200 m, expansion cooling takes the system on long excursions to lower temperatures, eventually reaching the liquid-gas phase boundary. At the liquid-gas phase boundary, there are two CO_2 phases (liquid and gas) in equilibrium with an aqueous phase. In this situation, three-phase relative permeability and capillary pressure functions are needed to model flow in the system as discussed in *Approach* and shown in Table 2.

Figure 14 shows a vertical saturation profile along the LHS of the system in P-T space at four different times. We have plotted in Figure 14 the CO_2 gas saturation and CO_2 liquid saturation in the body and outline of the plotted symbols, respectively, and the aqueous phase (brine) saturation by the color of the line connecting the symbols. One can see clearly here the migration of the system at discrete times to the liquid-gas phase boundary, and the persistence of three-phase conditions. To understand the evolution of the system, please see animated time plots in the Supplementary Material.

In general, it is known that evolving multiphase systems tend to stay on the liquid-gas phase boundary as suggested by the Gibbs Phase Rule which states that $Np + Nf = Nc + 2$, where Np is the number of phases, Nf is the number of degrees of freedom, and Nc is the number of components. Considering only the P-T plane of the pure CO_2 part of the H_2O-NaCl-CO_2 system, we have $Nc = 1$, $Nf = 3 - Np$. Therefore, when the system reaches the liquid-gas phase boundary, and two CO_2 phases occur, $Nf = 1$ and the system is restricted to following the liquid-gas phase boundary with only one degree of freedom, i.e., P and T are not free to vary independently. Only

when one phase is entirely consumed do we have $Nf = 3 - 1 = 2$ allowing the system to leave the liquid-gas phase boundary and evolve with two degrees of freedom (i.e., P and T independent). We see this behavior in Figure 14 by the P-T path that migrates to the liquid-gas phase boundary and then stays there. Examination of the colors of the symbol body, outline, and connecting line allows tracking of the phase evolution along the profile. On the liquid-gas phase boundary, as liquid CO_2 evolves, temperature increases as latent heat is produced, whereas gas evolution causes T to decrease. But the system is restricted to move up or down the phase boundary by the phase rule as long as both liquid and gaseous CO_2 exist. In the case considered here with an insulated RHS boundary and strong expansion cooling, the locations with co-existing liquid and gaseous CO_2 persist (stay on the liquid-gas phase boundary) and expand upward in the column until the temperature goes out of range of ECO2M ($T < 3$ °C).

Fixed geothermal gradient boundary, bubble rise

Finally we consider the case of a bubble of CO_2 rising upward in a narrow vertical conduit with a closed and constant-temperature bottom boundary and fixed geothermal gradient sidewall boundary condition. These results can be simulated using TOUGH2/ECO2N as no liquid CO_2 conditions occur. The main difference between this scenario and the constant injection scenario is that the bubble-rise case requires the use of hysteretic capillary pressure P_{cap} and relative permeability k_r because part of the system is undergoing CO_2 invasion (the top of the rising bubble) and part is undergoing water imbibition (the bottom of the rising bubble). Often in numerical simulation studies, one can devise any initial condition desired and start the simulation from that arbitrary state. It is interesting to note that in this case, we could not use this approach of emplacing an arbitrary bubble in the domain because we would not know which branch of the hysteretic P_{cap} and k_r curves we were on because the bubble did not have a wetting or drying history; in fact, it would have had no history at all. Instead, in cases where hysteretic P_{cap} and k_r are used, we need to begin the simulation with a brine-saturated system and then inject CO_2 to create a two-phase bubble. In this case, the injection rate was 1.58×10^{-2} kg/s across the entire domain at z = -450 m for 5 d (4.32×10^5 s) resulting in the CO_2 bubble occupying approximately 330 m in the center part of the domain. Gravity acts on this bubble causing it to rise with time.

Shown in Figure 15 are results after 5 d (at end of injection). The transition from supercritical to gaseous CO_2 occurs at approximately -320 m and the fixed geothermal gradient boundary condition is imparting some lateral variations in temperature and density as the bubble rises. Figure 16 shows results at t = 10 d, a time after which the bubble has broken through out the top but before the bubble has become completely immobile. As with the constant injection case, the results can be understood better by looking at vertical profiles over time as shown in Figure 17. The overall behavior as shown by the saturation profile is that of a finite-sized bubble rising upward and becoming distended as the trailing parts experience lower relative permeability than the leading parts for the same saturation (see Figure 3), and finally becoming static at about 15 days, as the saturation decreases to the residual saturation. This illustrates well the concept of

residual gas trapping, and makes the point that finite-sized bubbles cannot migrate infinitely far; rather, they spread out and become regions of residually trapped CO_2.

To illustrate this spreading/trapping effect further, simulations that injected smaller CO_2 bubbles were conducted, by injecting at the same rate as in the basic bubble-rise case, but for shorter time periods (1, 2, 3, or 4 days). Results indicate that smaller bubbles move a shorter distance before becoming trapped, and trapping occurs sooner after injection ends, as shown in Figure 18, which compares saturation profiles of different size bubbles at the end of their injection period and in their final trapped state. Only for the original 5-day injection does the CO_2 bubble reach the top of the column.

From Figure 18, it is apparent that to first order, the upward extent of the trapped plume could be simply predicted from the end-of-injection plume. We would first approximate the end-of-injection profile as having a constant saturation, then use the Land[16] equation to determine a single value of residual gas saturation S_{gr} for the whole profile. Next, we would assume that the steady-state profile had a constant saturation equal to S_{gr}. If CO_2 density were assumed to be constant, then we could predict the upward extent of the trapped CO_2 simply by conserving the area under the CO_2 saturation profiles. This simple calculation neglects CO_2 dissolution in the aqueous phase, and saturation and density variations with depth (Figure 17), making numerical simulation a more robust means of predicting plume extent, in addition to providing information on the timing of trapping. In fact, Figure 18 shows that, for the largest plume size, the steady-state CO_2 saturation (~0.04) is significantly smaller than S_{gr} (~0.07), but as plume size decreases, steady-state CO_2 saturation increases to S_{gr}. The explanation is as follows. For the larger plumes, when CO_2 injection ends, pressure decreases significantly (compare Figures 17a and 17b), and the CO_2 saturation decrease to S_{gr} (arising because of the difference in relative permeability at the leading and trailing edges of the plume) occurs under low pressure conditions (Figure 17b). When pressure subsequently increases back to the initial pressure profile (Figures 17c and 17d), CO_2 density and dissolution increase, with both processes resulting in a decrease in saturation that occurs despite the fact that CO_2 is immobile. As plume size decreases, the pressure oscillation decreases, leaving steady-state CO_2 saturation closer to S_{gr}.

Finally, we show in Figure 19 the *P-T* paths at five locations in the domain for the rising bubble case. These paths are more compact than those for the constant-injection case because the bubble rises past the observation points and the system comes to a new steady state with residually trapped CO_2 within the 30-day simulation period. Expansion cooling is visible in the results, but it is not large enough to bring the system over to the liquid-gas phase boundary and cause the formation of liquid CO_2. We omit simulations of the bubble-rise scenario with insulated outer-wall boundary because our concept of the bubble is that it is finite, e.g., rising in a conduit, and therefore the insulated boundary condition is not applicable.

Discussion

The results presented above apply directly to the prediction and design of long-column flow experiments focused on understanding upward CO_2 migration processes related to GCS. Many aspects of the system are idealized for practical experimental purposes, for example the high permeability and homogeneity of the sand was chosen so that flow would occur over practical time-scales for researcher convenience. These features of the model system limit the degree to which observations made in the simulations can be extrapolated to behaviors in natural systems. For example, the magnitude of the Joule-Thomson coefficient depends on *P-T* conditions and for typical reservoir conditions is 7.5 ^{o}C MPa^{-1} [29]. A hydrostatic ΔP across 500 m of 5 MPa would thus yield a temperature drop of 7.5 ^{o}C MPa^{-1} × 5 MPa = 37.5 ^{o}C. With an initial temperature around 40 °C, it is expected that the fluid could cool into the single digits if heat transfer from the surrounding rock did not occur. Rock-fluid heat transfer is minimized by the high porosity (high fluid to rock matrix ratio) and permeability (fast upward flow) of the LCPV sand, which likely over-estimate the effect of expansion cooling that would be observed in natural systems.

Nevertheless, many aspects of the results are relevant to natural systems. Specifically, the results confirm that the upward flow of CO_2 in a narrow conduit will be much more influenced by the thermal conditions of the surrounding ambient formations than will upward flow in the middle of a large CO_2 plume. The result of this difference is that more of the expansion-cooling and phase-change thermal effects will occur in the middle of an upward-flowing CO_2 plume than in a leaking well or fault zone where the temperature of the surrounding formation dominates over the intrinsic thermodynamically controlled temperature. As such, we speculate that liquid CO_2 conditions are very likely to occur at depths of approximately 700 m in upward-flowing CO_2 plumes over vertical distances in which the supercritical to gaseous CO_2 transition occurs. The reason is that expansion cooling will be sufficient in these cases to drive the system to the liquid-gas phase boundary where CO_2 liquid is stable. Pruess [24] noted strong phase interference effects and latent heat effects led to oscillatory leakage fluxes for a system with a narrow fault leakage pathway connected to a saline reservoir. The full implications of the occurrence of liquid CO_2 were not investigated here and will need further study.

Another result that is applicable to natural systems is the occurrence of residual gas trapping for the bubble-rise case. As expected, a large fraction of the injected CO_2 becomes trapped in the trailing edge of the bubble, even in an unconsolidated sand column with 40% porosity and nearly 20 Darcy permeability. For lower permeability media, residual trapping is expected to increase as the CO_2 residual saturation S_{gr} increases. S_{gr} is a history-dependent property that is correlated to the maximum historical CO_2 saturation S_{gmax}, and the maximum possible CO_2 residual saturation S_{grmax}, a fixed material property, through the Land[16] equation. Both S_{gmax} and S_{grmax} tend to increase as permeability is decreased, resulting in much larger values of S_{gr}. Large-scale experiments and simulations focused on determining the sensitivity of residual trapping to the various textural aspects of porous media will complement prior and ongoing laboratory

measurements and experiments (e.g., Bachu and Bennion[30]; Perrin and Benson[31]; Krevor et al.[32]).

The simulations carried out in this study revealed a gaping hole in our knowledge about three-phase relative permeability relevant to GCS. We assumed a Parker et al.[11] three-phase relative permeability model, which honors the aqueous phase relative permeability suggested by the Rosetta database[9]. The database does not include any information for the gas and liquid CO_2 relative permeabilities, which is in keeping with the generic functions for gas and liquid CO_2 relative permeabilities incorporated in the Parker et al.[11] model. We ran many other cases with different three-phase relative permeability functions and these often produced different results from the Parker et al. [11] cases. Second, hysteresis in three-phase systems may be important in some cases, and yet accepted models for hysteretic three-phase relative permeability are not available. There is a clear need for experiments, such as those that could be carried out at LUCI, for defining complex multiphase flow model parameters such as these.

Finally, we emphasize that while the simulations presented here are rigorous implementations of physical laws and property descriptions to the extent they are known, nothing will demonstrate their validity like an actual large-scale experiment. And in all likelihood, a large-scale experiment would reveal additional unpredicted behaviors the study of which could allow increased understanding of large-scale flow and phase change phenomena in CO_2 systems. Such a facility needs to provide confinement for pressures up to 10 MPa or more over a large vertical extent, permit injection and collection of fluid at the top and bottom under controlled-pressure and temperature conditions, and be able to have either isothermal or insulated boundary conditions along the outer sidewall. In the course of the last year, the prospects for funding the construction of LUCI at DUSEL have dimmed considerably, forcing us to look actively for other opportunities for siting LUCI.

Conclusions

Numerical simulations using TOUGH2/ECO2M and ECO2N of long-column flow experiments such as those proposed for LUCI have been carried out. In order to represent various natural upward flow scenarios, boundary conditions must be chosen for the outer wall of the effectively one-dimensional flow system. The fixed geothermal gradient boundary condition is representative of the case of CO_2 flow up a narrow conduit such as the annulus of an abandoned well or a fault zone. The insulated boundary condition is representative of the upward flow of CO_2 in the middle of a much larger CO_2 plume. Results for scenarios involving constant injection of CO_2 and the rise of a bubble of CO_2 in an initially brine-filled sand column show sensitivity to the outer wall thermal boundary condition. Radial gradients in temperature occur for the fixed geothermal gradient case showing the outer wall temperature controls the temperature in the system whereas in the insulated case heat transfer and temperature are controlled by vertical advection and conduction, expansion, and phase change processes.

Liquid CO_2 forms in flow simulations using either boundary condition, but much more liquid forms in the insulated outer wall case because expansion cooling is stronger when the outer wall boundary does not supply heat to the system. When two-phase liquid-gas conditions occur, the system is locked on the liquid-gas phase boundary consistent with Gibbs Phase Rule.

The prevalence of liquid CO_2 in these upward-leakage simulations motivates the development of LCPVs in which controlled flow and reactive transport experiments can be carried out. While the model system considered here was quite simple, complex thermal and phase-change processes were observed. An experimental facility would provide the opportunity for researchers to investigate outstanding research questions such as the role of phase interference in multiphase CO_2 systems along with much more realistic and complex systems, for example by layering different materials into the column. We are actively looking for opportunities to help develop such a large-scale experimental facility.

Acknowledgment

We thank Joe Wang (LBNL) for support and encouragement of underground laboratory science, and Stefan Finsterle (LBNL) for internal review of an earlier draft. We are indebted to two anonymous reviewers whose careful scrutiny and questioning of results allowed us to improve the presentation. This work was supported by the National Science Foundation under Grant Numbers CMMI-0965552 (to LBNL) & CMMI-0919140 (to Princeton University), and by Lawrence Berkeley National Laboratory under Department of Energy Contract No. DE-AC02-05CH11231.

References

1. Pruess K. On CO_2 fluid flow and heat transfer behavior in the subsurface, following leakage from a geologic storage reservoir. *J Environ Geol* **54:** 1677-1686 (2007).

2. De la Reguera D, Stute M, Matter JM. Laboratory experiments on CO_2 dissolution in water for carbon sequestration. Proceedings of the American Geophysical Union EOS, 2010 Dec 13-17, San Francisco, CA (2010).

3. Carlson MR. Practical Reservoir Simulation, Using, Assessing, and Developing Results. PennWell Books, Tulsa, Oklahoma, 564 pp (2003).

4. Maloney DR, Briceno M. Experimental investigation of cooling effects resulting from injecting high pressure liquid or supercritical CO_2 into a low pressure gas reservoir. Proceedings of the International Symposium of the Society of Core Analysts held in Abu Dhabi, UAE, 29 October-2 November 2008.

5. Peters CA, Dobson PF, Oldenburg CM, Wang JSY, Onstott TC, Scherer GW, et al. LUCI: A facility at DUSEL for large-scale experimental study of geologic carbon sequestration. LBNL-3983E. *Energy Procedia*, 2, Elsevier, GHGT-10, Sept. 19–23, 2010, Amsterdam, The Netherlands (2010).

6. Gasda SE, Bachu S, Celia MA. Spatial characterization of the location of potentially leaky wells penetrating a deep saline aquifer in a mature sedimentary basin. *J Environ Geol* **46(6-7):** 707-720 (2004).

7. House KZ, Harvey CF, Aziz MJ, Schrag DP. The energy penalty of post-combustion CO_2 capture & storage and its implications for retrofitting the U.S. installed base. *Energy & Environmental Science* **2:** 193-205 (2009).

8. Lesko KT. The US National Science Foundation's deep underground laboratory at Homestake- DUSEL. *J Physics*: Conference Series 120, 052011 (2008).

9. Schaap MG. Rosetta Version 1.2. U.S Salinity Laboratory ARS-USDA (2000).

10. De Marsily G. Quantitative Groundwater Hydrology. New York: Academic Press, 440 pp (1986).

11. Parker JC, Lenhard RJ, Kuppusamy T. A parametric model for constitutive properties governing multiphase flow in porous media. *Water Resources Research* **23(4):** 618- 624 (1987).

12. Doughty C. Modeling geologic storage of carbon dioxide: Comparison of non-hysteretic and hysteretic characteristic curves. *Energy Conversion and Management* **48(6):** 1768–1781 (2007).

13. Niemi A, Bodvarsson GS. Preliminary capillary hysteresis simulations in fractured rocks, Yucca Mountain, Nevada. *J Contam Hydrol* **3:** 277–291 (1988).

14. Finsterle S, Sonnenborg TO, Faybishenko B. Inverse modeling of a multistep outflow experiment for determining hysteretic hydraulic properties. In: K. Pruess, editor. Proceedings of the TOUGH workshop'98, Lawrence Berkeley National Laboratory Report LBNL-41995, May 1998, p. 250–256.

15. van Genuchten M Th. A closed-form equation for predicting the hydraulic conductivity of unsaturated soils. *Soil Science Society of America J* **44(5):** 892–898 (1980).

16. Land CS. Calculation of imbibition relative permeability for two- and three-phase flow from rock properties. *Society of Petroleum Engineers J* **8(2):** 149–156 (1968).

17. Mualem Y. A modified dependent domain theory of hysteresis. *Soil Science* **137(5):** 283–291 (1984).

18. Parker JC, Lenhard RJ. A model for hysteretic constitutive relations governing multiphase flow, 1. Saturation-pressure relations. *Water Resources Research* **23(12):** 2187–2196 (1987).

19. Lenhard RJ, Parker JC. A model for hysteretic constitutive relations governing multiphase flow, 2. Permeability-saturation relations. *Water Resources Research* **23(12):** 2197–2205 (1987).

20. Pruess K, Oldenburg CM, Moridis GJ. TOUGH2 User's Guide Version 2. November 1999, Lawrence Berkeley National Laboratory Report LBNL-43134 (1999).

21. Pruess K. The TOUGH Codes—A Family of Simulation Tools for Multiphase Flow and Transport Processes in Permeable Media. *Vadose Zone* J **3:** 738-746 (2004).

22. Pruess K. ECO2N: A TOUGH2 fluid property module for mixtures of water, NaCl, and CO_2. August 2005, Lawrence Berkeley National Laboratory Report LBNL-57952 (2005).

23. Pruess K, Spycher N. ECO2N – A Fluid Property Module for the TOUGH2 Code for Studies of CO_2 Storage in Saline Aquifers. *Energy Conversion and Management* **48(6):**1761–1767 (2004).

24. Pruess K. Integrated modeling of CO_2 storage and leakage scenarios including transitions between super- and subcritical conditions, and phase change between liquid and gaseous CO_2. *Greenhouse Gases: Science and Technology* **1(3):** 237–247 (2011).

25. Pruess K. ECO2M: A TOUGH2 fluid property module for mixtures of water, NaCl, and CO_2, including super- and sub-critical conditions, and phase change between liquid and gaseous CO_2. May 2011, Lawrence Berkeley National Laboratory Report LBNL-4590E (2011).

26. Waldbaum DR. Temperature changes associated with adiabatic decompression in geological processes. *Nature* **232:** 545-547 (1971).

27. Ramberg J. Comment on Temperature changes associated with adiabatic decompression in geological processes. *Nature* **234:** 539-540 (1971).

28. Stauffer P, Stein J, Travis B. The correct form of the energy balance for fully coupled thermodynamics in water. Los Alamos National Laboratory Report LA-UR-03-1555, 9 pp (2003).

29. Oldenburg CM. Joule-Thomson cooling due to CO_2 injection into natural gas reservoirs. *Energy Conversion and Management* **48:** 1808-1815 (2007).

30. Bachu S, Bennion B. Effects of in-situ conditions on relative permeability characteristics of CO_2-brine systems. *J Environ Geol* **54(8):** 1707-1722 (2008).

31. Perrin J-C, Benson SM. An experimental study on the influence of sub-core scale heterogeneities on CO_2 distribution in reservoir rocks. *Transport in Porous Media* **82(1):** 93-109 (2009).

32. Krevor S, Pini R, Li B, Benson S. Capillary heterogeneity trapping of CO_2 in a sandstone rock at reservoir conditions. *Geophysical Research Letters* 38, L15401 (2011).

Tables

Table 1. Boundary conditions used for the model system.

Boundary	Pressure (MPa)	Temperature (°C)	Comment
LHS	Closed	Insulated	We are assuming very little thermal forcing from the inner access well because of the small volume and because the system is mirrored on the other side, and because vertical convection could be suppressed, if necessary, by insertion of appropriate tools and baffles.
Bottom	Closed	Insulated	CO_2 injection occurs along the bottom for the constant-injection cases and is closed for the rising-bubble cases.
RHS	Closed	Case 1: Constant *T* equal to geothermal gradient; Case 2: Insulated	The flow region is actually separated from the numerical boundary condition by an impermeable stainless steel sidewall of thickness 5 cm.
Top	Open (constant *P* equal to 350 m * 9.81 m/s^2 * 1000 kg/m^3 = 3.43 MPa)	Constant *T* (15 °C + 0.35 km (25 °C/km) = 23.75 °C)	Flow is always out of the top boundary for the constant-injection cases. Brine may flow back into the system from top after passage of the CO_2 bubble in the

			bubble-rise scenarios.

Table 2. Properties of the pure sand[9] and stainless-steel sidewall of the LUCI system.

Property	Value
Porosity (ϕ)	0.40
Permeability (k)	1.7×10^{-11} m^2
Capillary Pressure (P_{cap}) and Relative Permeability (k_r) *Terminology:* λ = m = 1-1/n = power in expressions for P_{cap} and k_r γ = power in hysteretic expression for k_{rg} $S_{ar} = S_m$ = aqueous-phase residual saturation S_{lr} = CO_2 liquid-phase residual saturation S_{gr}= CO_2 gas-phase residual saturation S_{grmax} = maximum possible CO_2 gas-phase residual saturation $P_{c0} = \alpha^{-1}$ = capillary pressure strength between aqueous and non-aqueous phases P_{cmax} = maximum possible value of P_{cap} k_{ra} = aqueous-phase relative permeability k_{rg} = CO_2 gas-phase relative permeability k_{rl} = CO_2 liquid-phase relative permeability	van Genuchten[1] hysteretic two-phase and Parker[2] non-hysteretic three-phase $\lambda = 0.774$ $\gamma = 0.5$ S_{ar} = 0.127 for P_{cap}, 0.130 for k_r S_{gr} = 0 for drainage, non-zero and history-dependent for imbibition[3] with $S_{grmax} = 0.15$ $S_{lr} = 0$ P_{c0} = 2875 Pa $P_{cmax} = 1 \times 10^6$ Pa P_{cap} between CO_2 gas, liquid, and supercritical phases is assumed to be zero.
Thermal conductivity of sand and brine mixture[4]	2.5 W/(m K)
Thermal conductivity of 5 cm-thick stainless steel (304) on RHS boundary	14.6 W/(m K)
Density of stainless steel	7920 kg/m^3
Heat capacity (C_P) of stainless steel	502.1 J/(kg K)

[1]van Genuchten[15], as implemented in Doughty [12], see Figure 3

[2]Parker et al.[11] as implemented in Pruess[25], simplifies to van Genuchten drainage when only two phases present

[3]Only significant for the bubble-rise case

[4]deMarsily[10], Table 10.4, p. 281

Figures

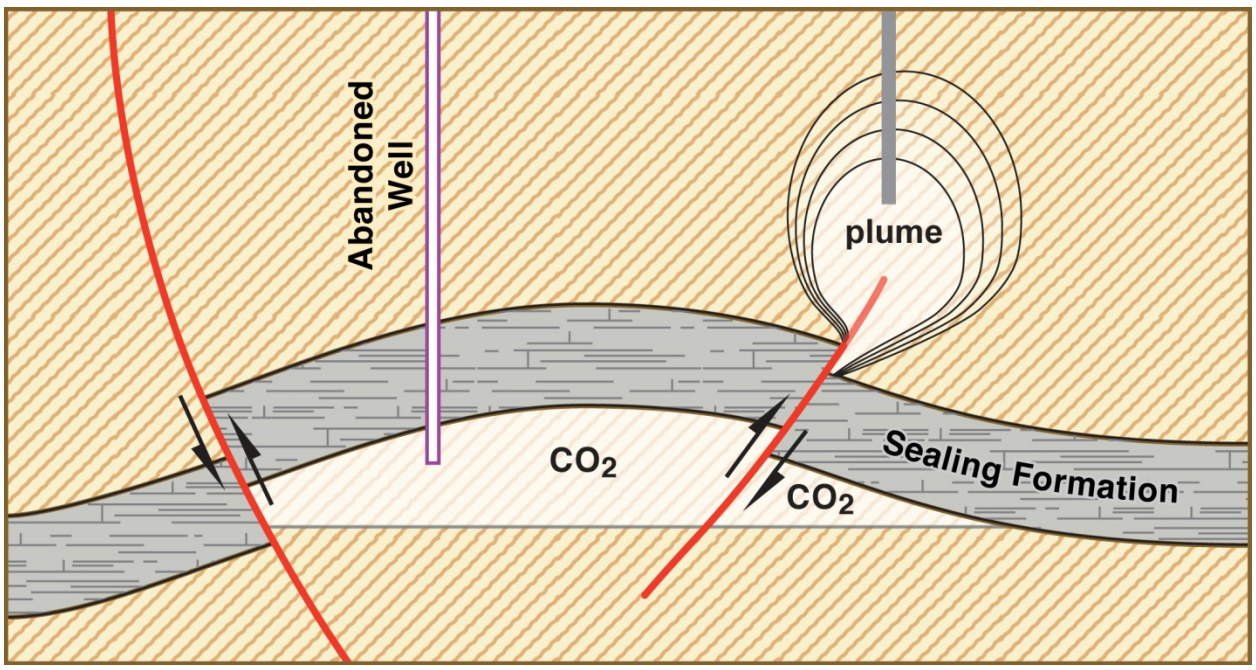

Figure 1. Conceptual models of fault and abandoned-well leakage pathways for CO_2. The one-dimensional nature of the leakage pathway is implicit in the abandoned well; for the CO_2 plume, the one-dimensional flow conceptualization is shown by the light gray bar which represents upward flow in the center of a large upwelling region.

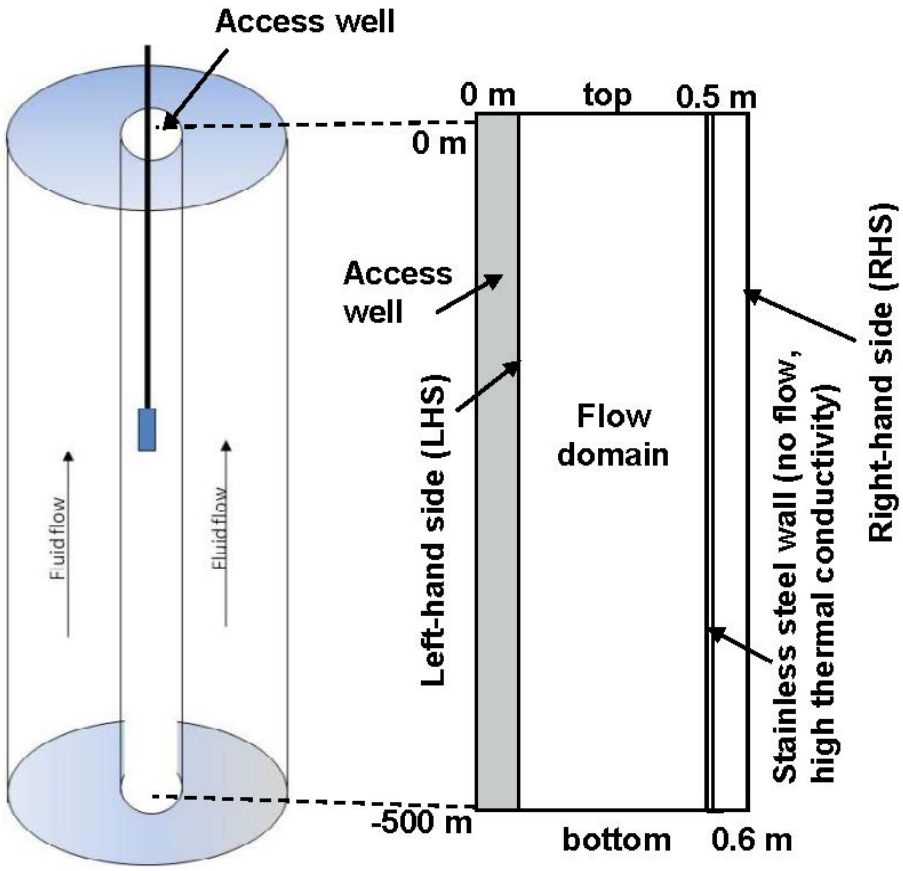

Figure 2. Sketch of annular flow region in long-column flow vessel, which includes an inner annulus for deployment of monitoring equipment. On the right-hand side is the two-dimensional radial numerical simulation domain with named boundaries (LHS = left-hand side (inner wall), RHS = right-hand side (outer wall)).

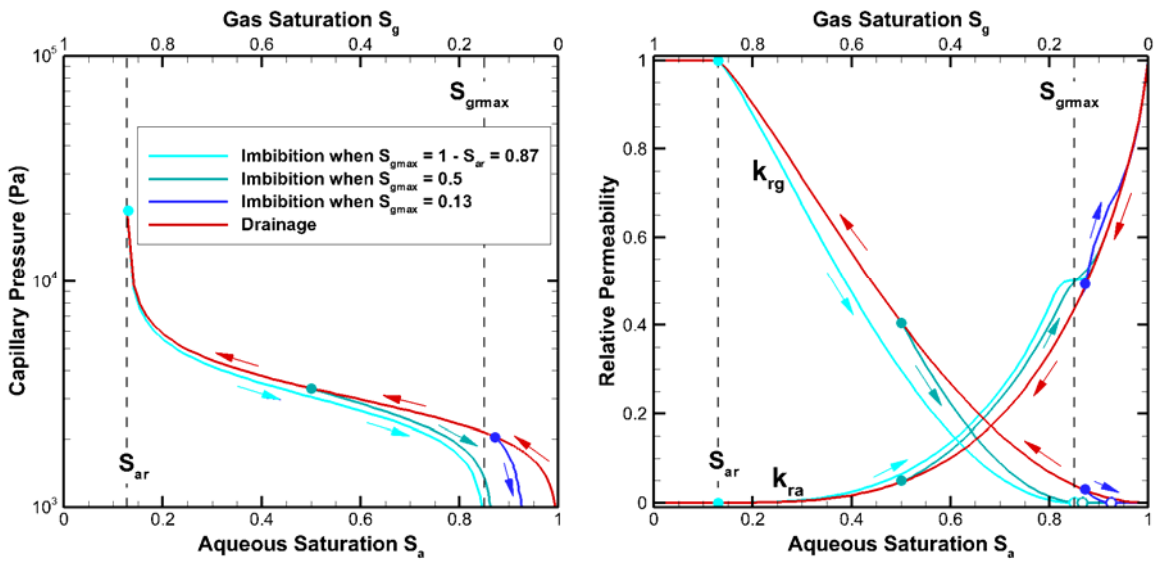

Figure 3. Hysteretic capillary pressure and relative permeability functions used in the modeling of the bubble-rise case. The simulation begins on the drainage branch as CO_2 is injected into the brine-filled LCPV. The closed circles show three possible values of maximum CO_2 saturation S_{gmax} (0.87, 0.5, 0.13), corresponding to the transition from drainage to imbibition that occurs some time after CO_2 injection ends (at different times for different parts of the plume). Thereafter, an imbibition branch is followed; the open circles in the lower right-hand corner of the relative permeability plot show the corresponding values of history-dependent residual gas saturation S_{gr}. For the present simulations, we find that S_{gmax} ranges from 0.11 to 0.13 over the entire length of the CO_2 bubble, for which the Land[16] equation produces $S_{gr} \sim 0.07$, as shown by the dark blue circle.

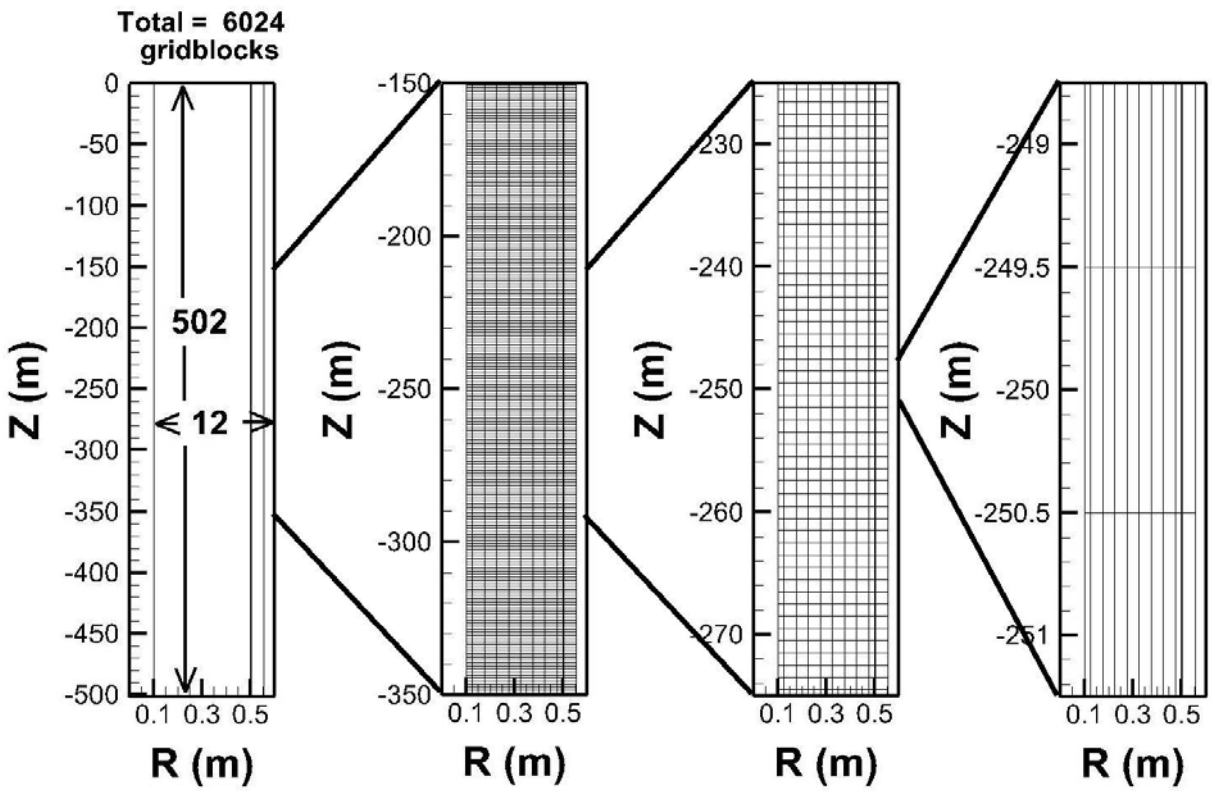

Figure 4. Discretization of the domain showing progressive blow-ups for clarity. Note the steel wall is located at R = 0.5 m, beyond which is part of the domain that maintains a constant temperature in the geothermal-gradient RHS boundary cases.

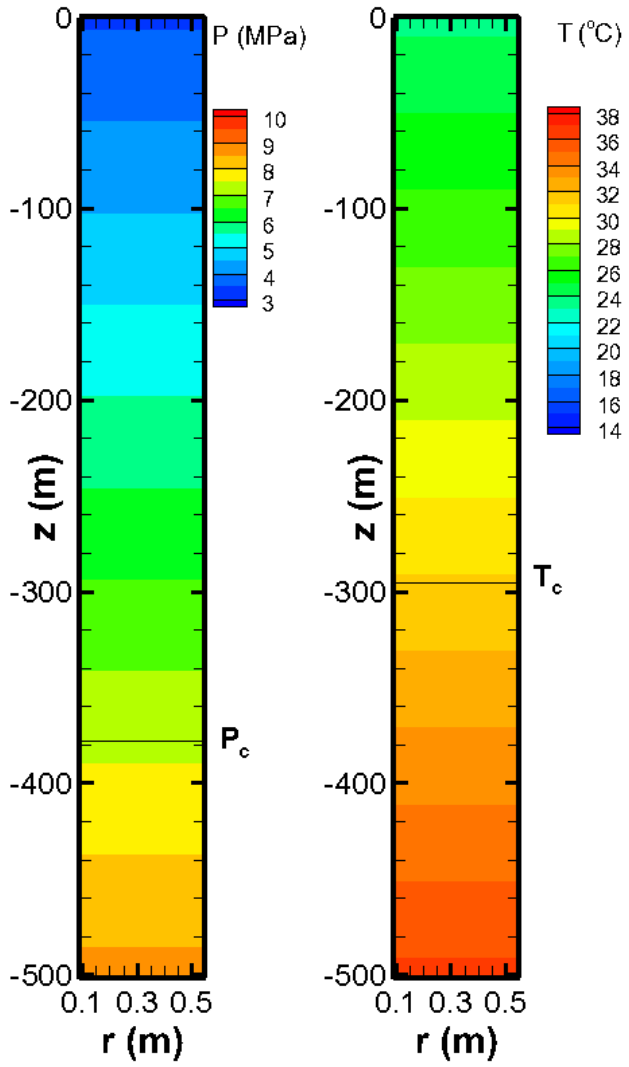

Figure 5. Initial conditions for the system are fully brine saturated (no CO_2 present) and hydrostatic *P* with geothermal-gradient *T* profile.

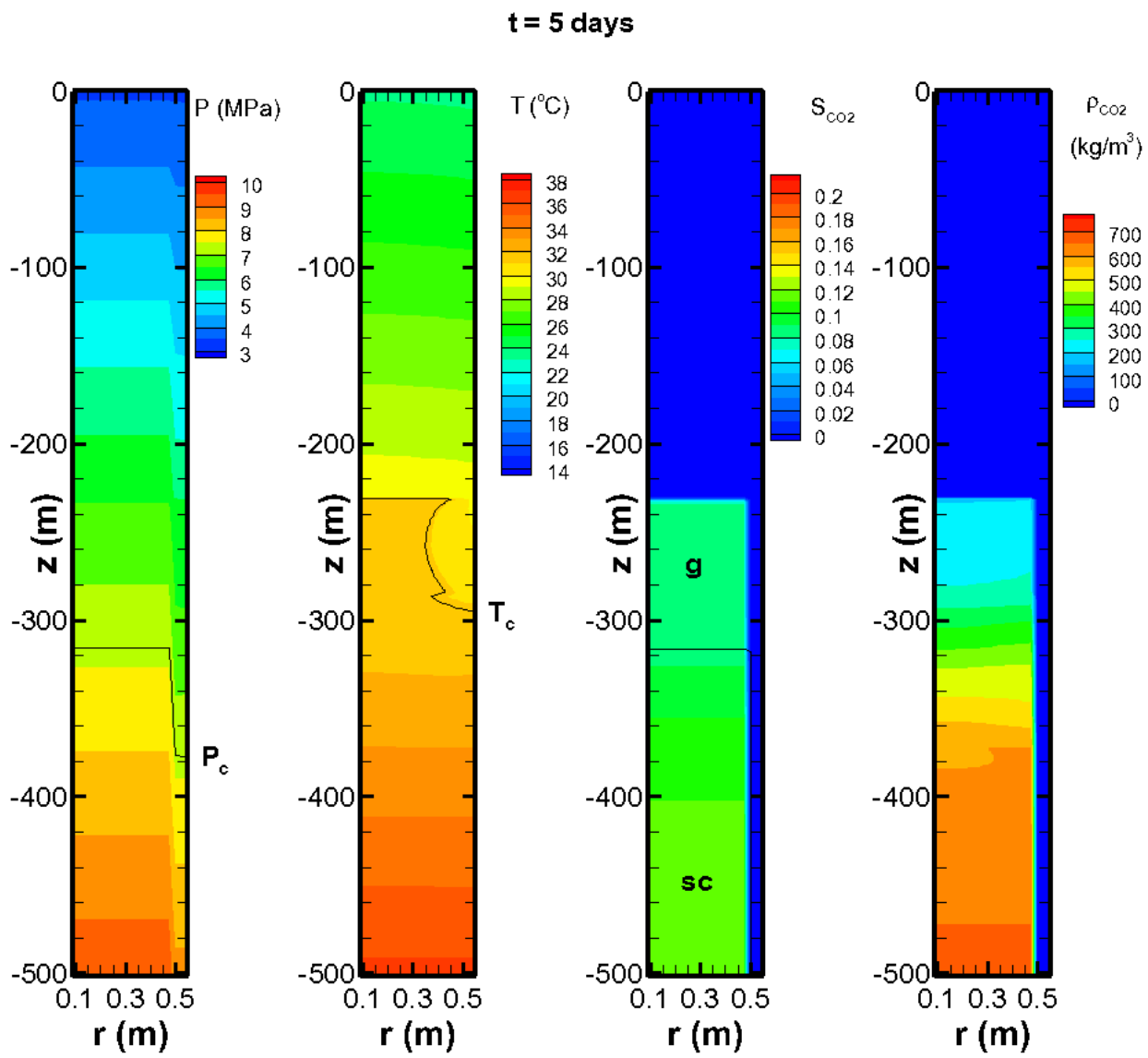

Figure 6. Simulation results for the constant-injection case at t = 5 d showing P, T, S_{CO2}, and ρ_{CO2} for the case of the fixed geothermal gradient boundary condition on the RHS. The critical pressure (P_c) and temperature (T_c) are indicated by the light solid curves on the P and T plots; CO_2 phase is identified as gas (g) or supercritical (sc) in the saturation plot. Note the pressure variation for r > 0.5 m is an artifact of the model that plays no role in the flow because the permeability of the steel sidewall is zero.

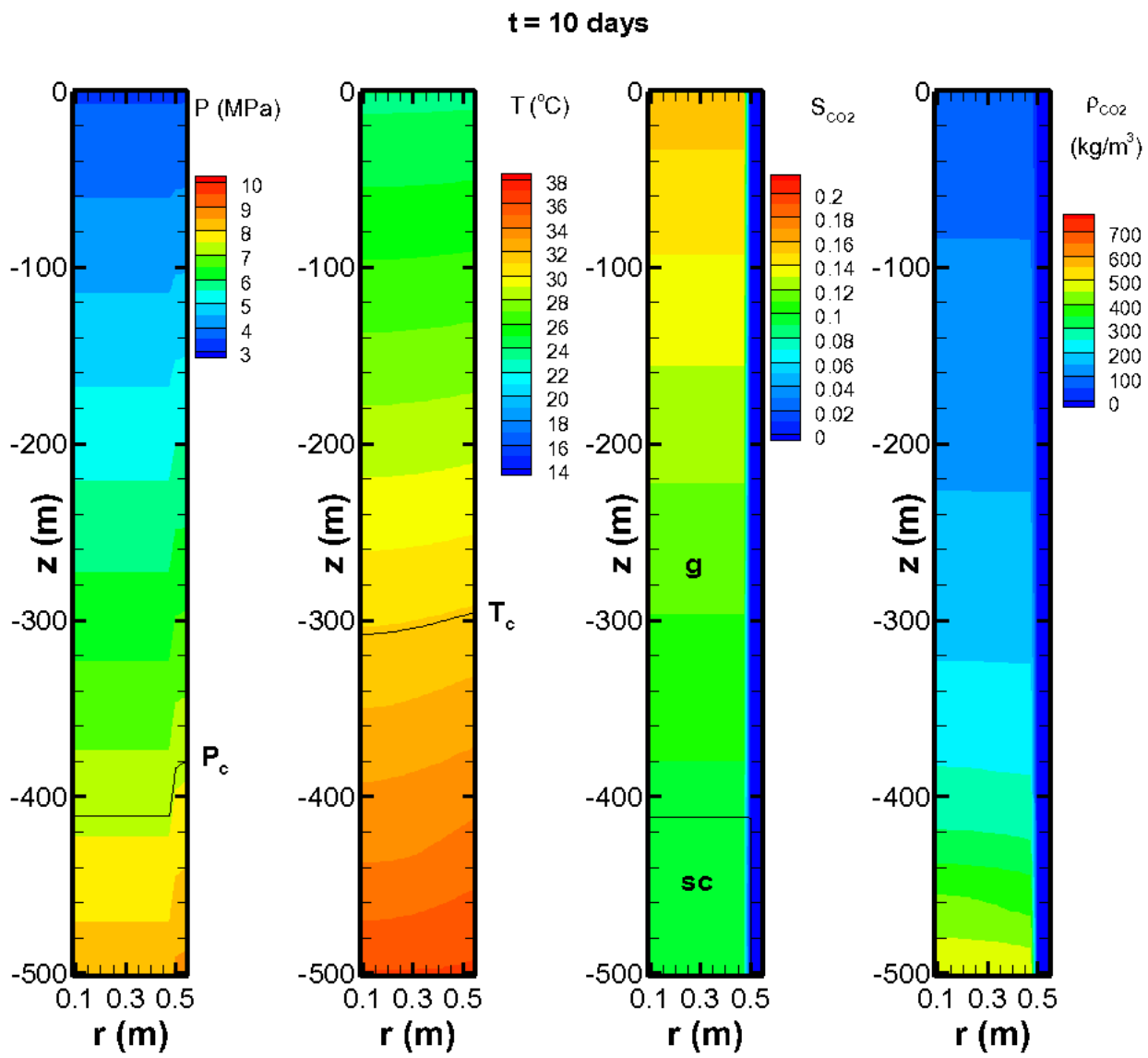

Figure 7. Simulation results for the constant-injection case at t = 10 d showing P, T, S_{CO2}, and ρ_{CO2} for the case of the fixed geothermal gradient boundary conditions on the RHS.

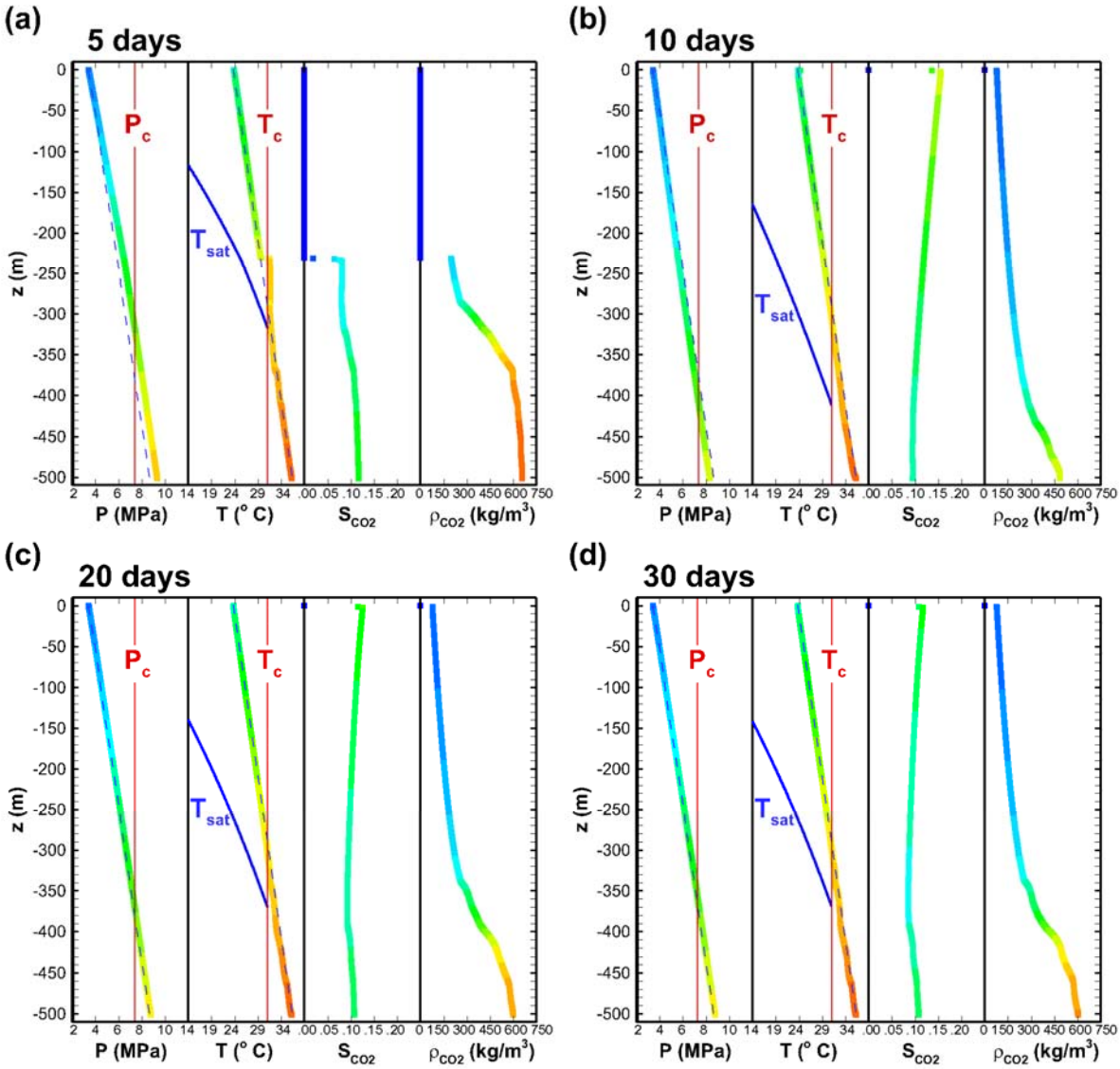

Figure 8. Vertical profiles along the inner radius of the domain at (a) t = 5 d, (b) t = 10 d, (c) t = 20 d, and (d) t = 30 d for the constant-injection case with a fixed geothermal gradient boundary condition on the RHS. The color of the lines represents the value of the variable being plotted against depth, for visual emphasis. Initial conditions for P and T are shown by the dashed lines. The liquid-gas phase boundary is shown in the temperature frame by the line labeled T_{sat}.

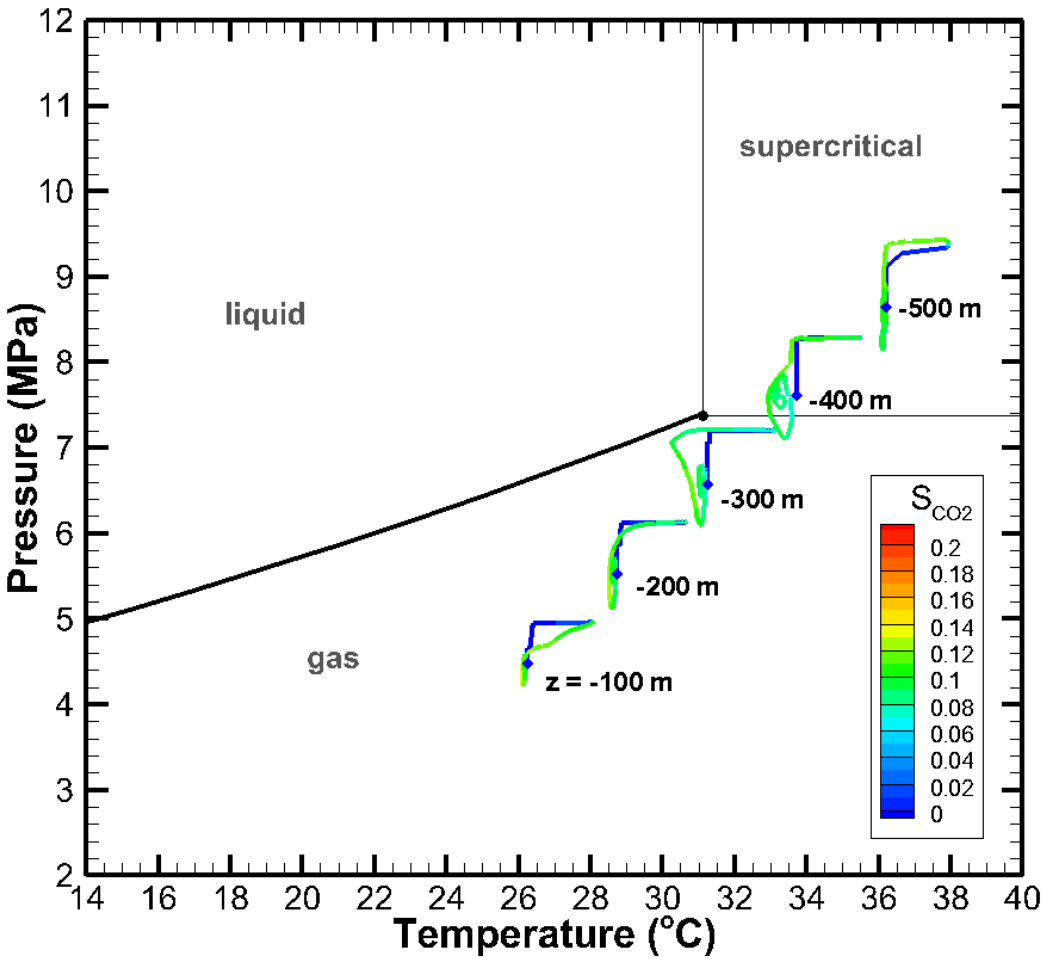

Figure 9. Trajectories over 40 days of *P*, *T*, and CO_2 saturation at five depths for the constant-injection case with a fixed geothermal gradient boundary condition on the RHS. The diamond symbols show initial conditions, while the line color represents CO_2 saturation.

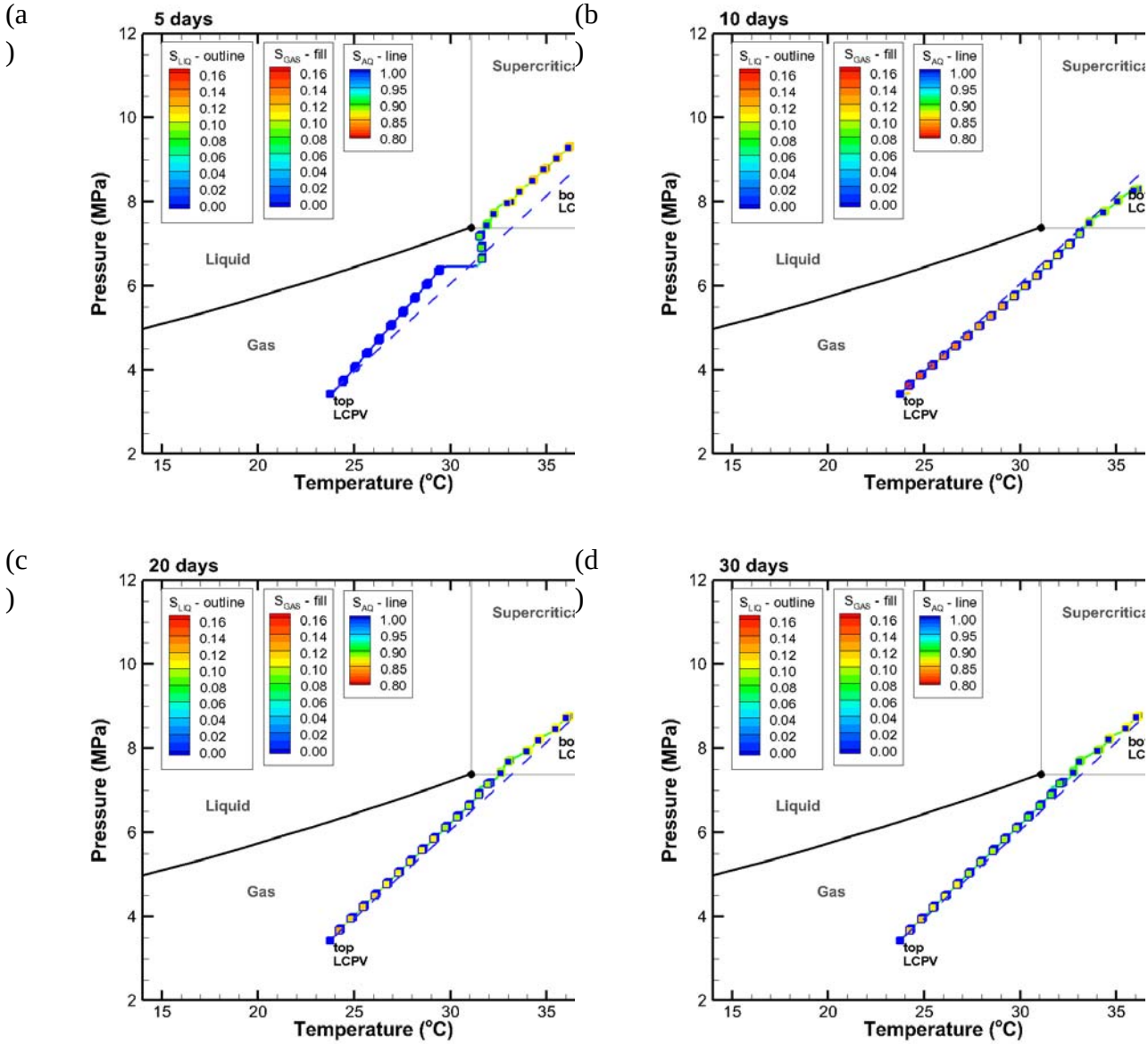

Figure 10. Vertical pressure and temperature profiles with saturations in *P-T* space through the domain at t = 5, 10, 20, and 30 days for the constant-injection case with a fixed geothermal gradient boundary condition on the RHS. The dashed line shows the initial conditions. The color of the outline of the symbols represents liquid or supercritical CO_2 saturation, the fill color represents gaseous CO_2 saturation, and the line color represents aqueous phase saturation with value ranges shown by the three legends. Note that the abrupt color change that occurs as the profile crosses the border between the supercritical and gas regions does not correspond to an abrupt change in properties, merely a change in nomenclature. Symbols show results for only a sub-set of grid blocks, to enable the outline and fill of each symbol, and the line connecting the symbols, to show. Animations of this *P-T* profile are available in Supplementary Material.

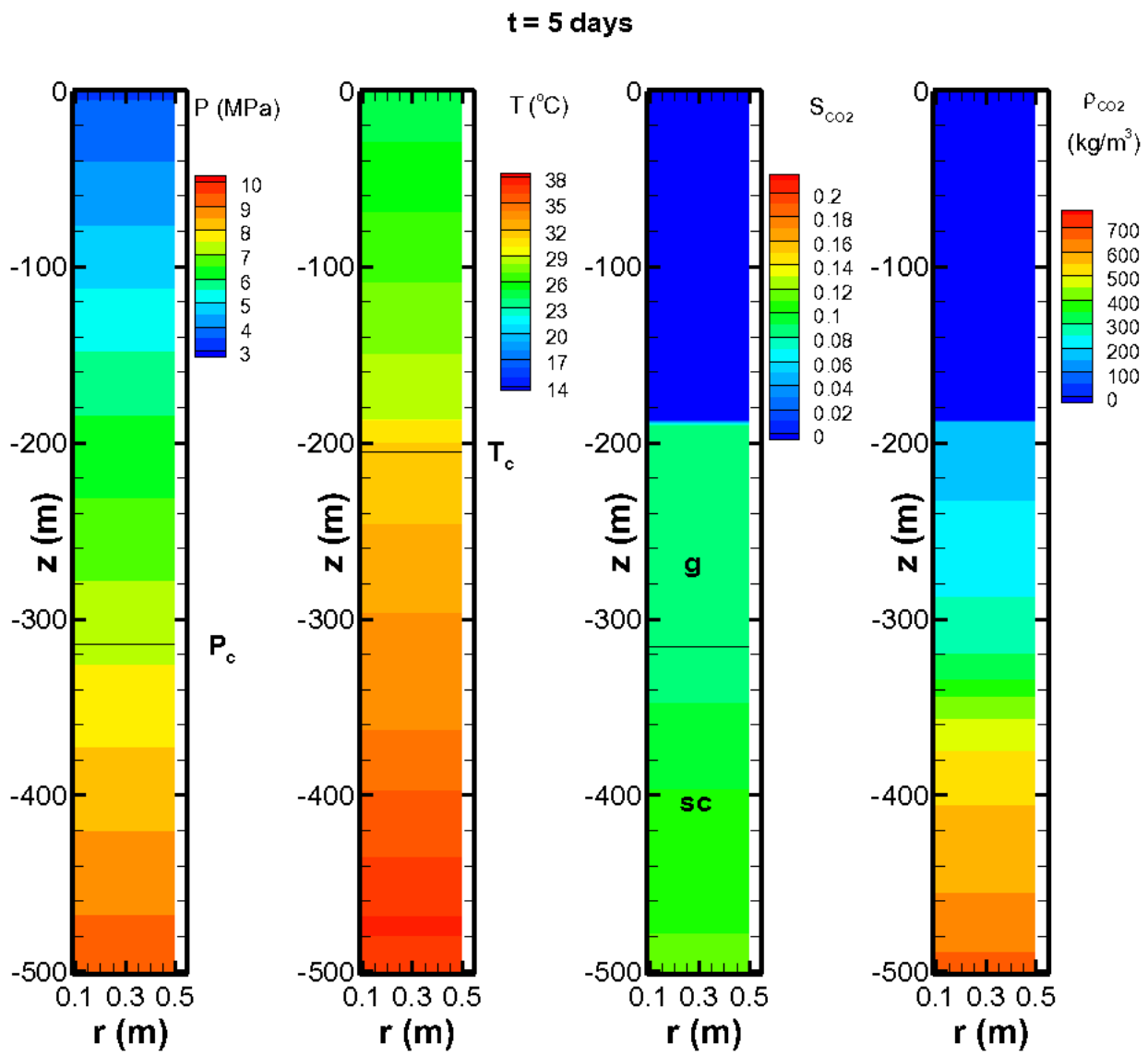

Figure 11. Simulation results for the constant injection case at t = 5 d showing P, T, S_g, and ρ_{CO2} for the case with an insulated boundary condition on the RHS (created by simply removing gridblocks with r > 0.5 m). Note that there is no variation in the lateral (r) direction (i.e., the fields are one-dimensional).

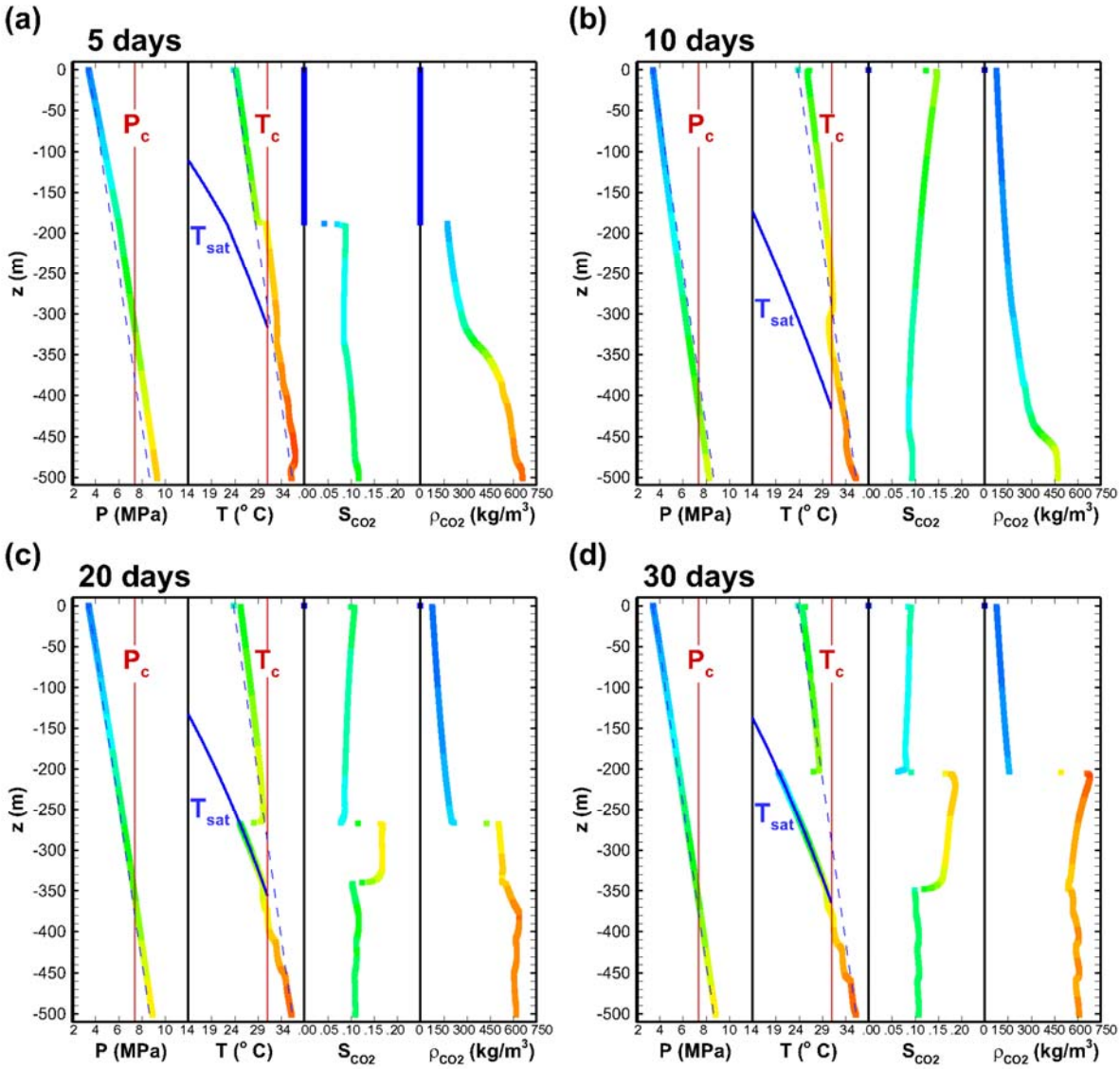

Figure 12. Vertical profiles along the inner radius of the domain at (a) t = 5 d, (b) t = 10 d, (c) t = 20 d, and (d) t = 30 d for the constant-injection case with an insulated boundary condition on the RHS.

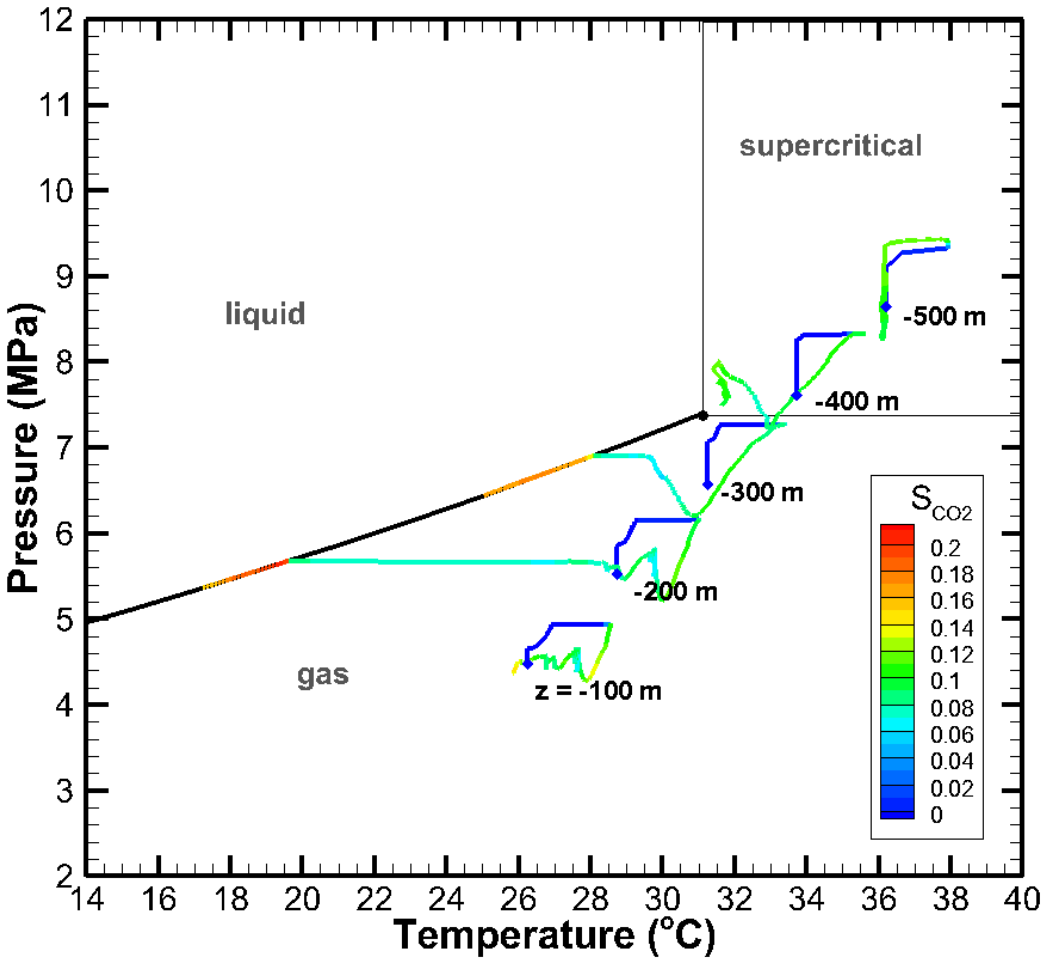

Figure 13. Trajectories over 40 days of *P*, *T*, and CO_2 saturation at five depths for the constant-injection case with an insulated outer wall boundary condition. The diamond symbols show initial conditions.

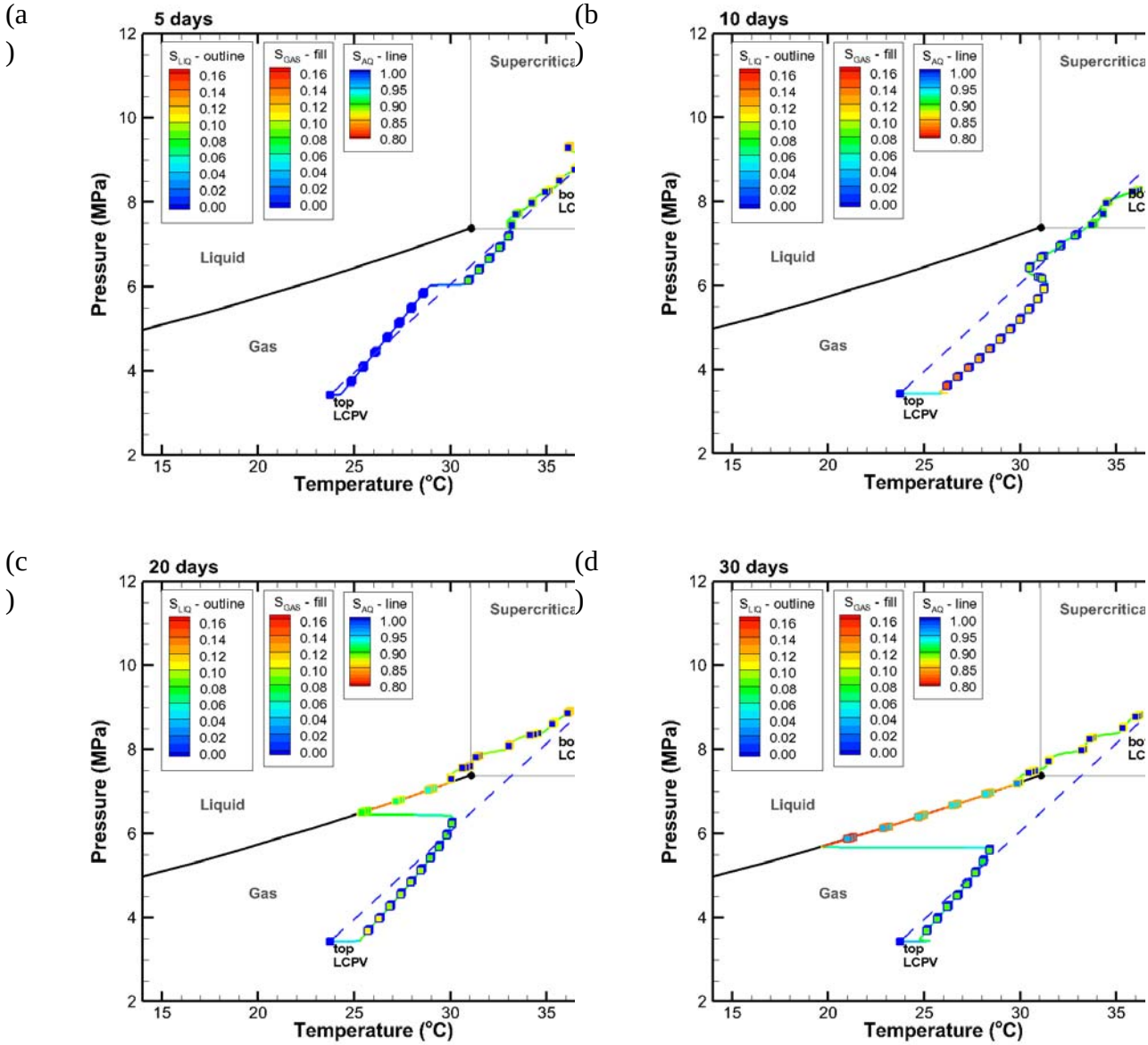

Figure 14. Vertical pressure and temperature profiles with saturations in *P*-*T* space through the domain at t = 5, 10, 20, and 30 days for the constant-injection case with an insulated RHS boundary. Animations of this *P*-*T* space profile are available in Supplementary Material.

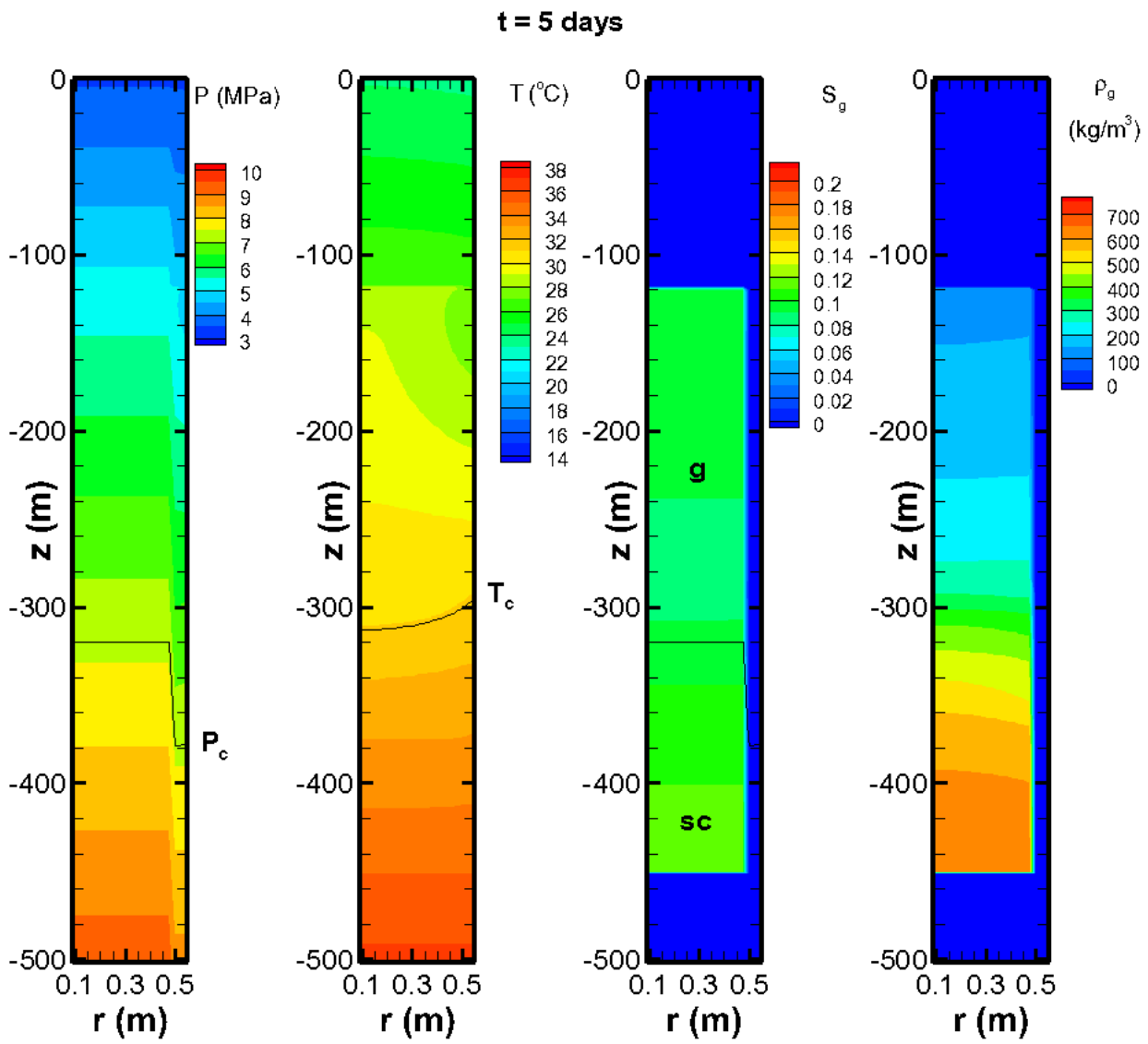

Figure 15. Simulation results for the bubble-rise case at t = 5 d and fixed geothermal gradient boundary condition on the outer wall (RHS).

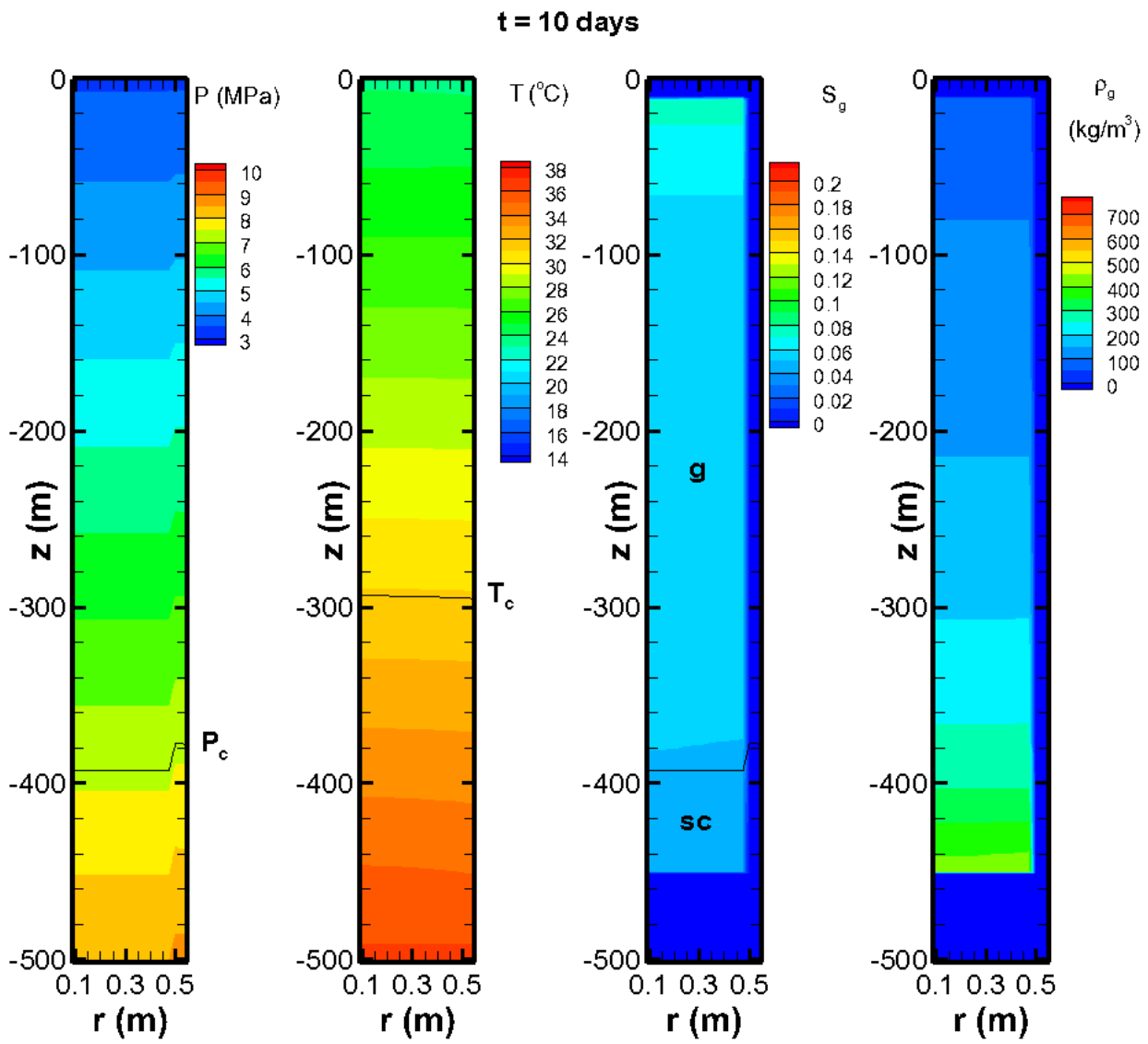

Figure 16. Simulation results for the bubble-rise case at t = 10 d showing the trapping of residual CO_2.

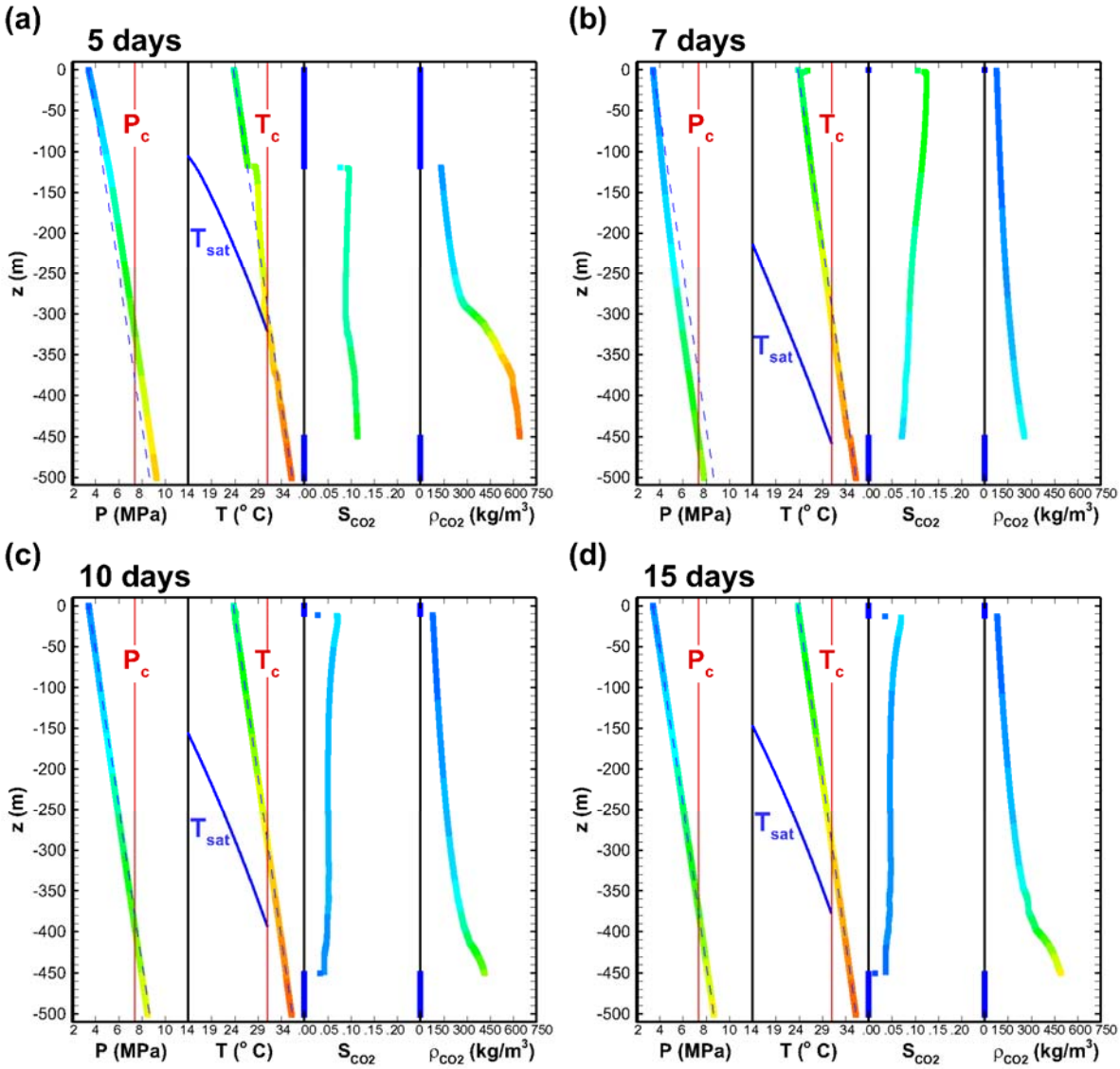

Figure 17. Vertical profiles along the inner radius of the domain for the bubble-rise case at (a) t = 5 d, (b) t = 7 d, (c) t = 10 d, and (d) t = 15 d. CO_2 is trapped at 15 d.

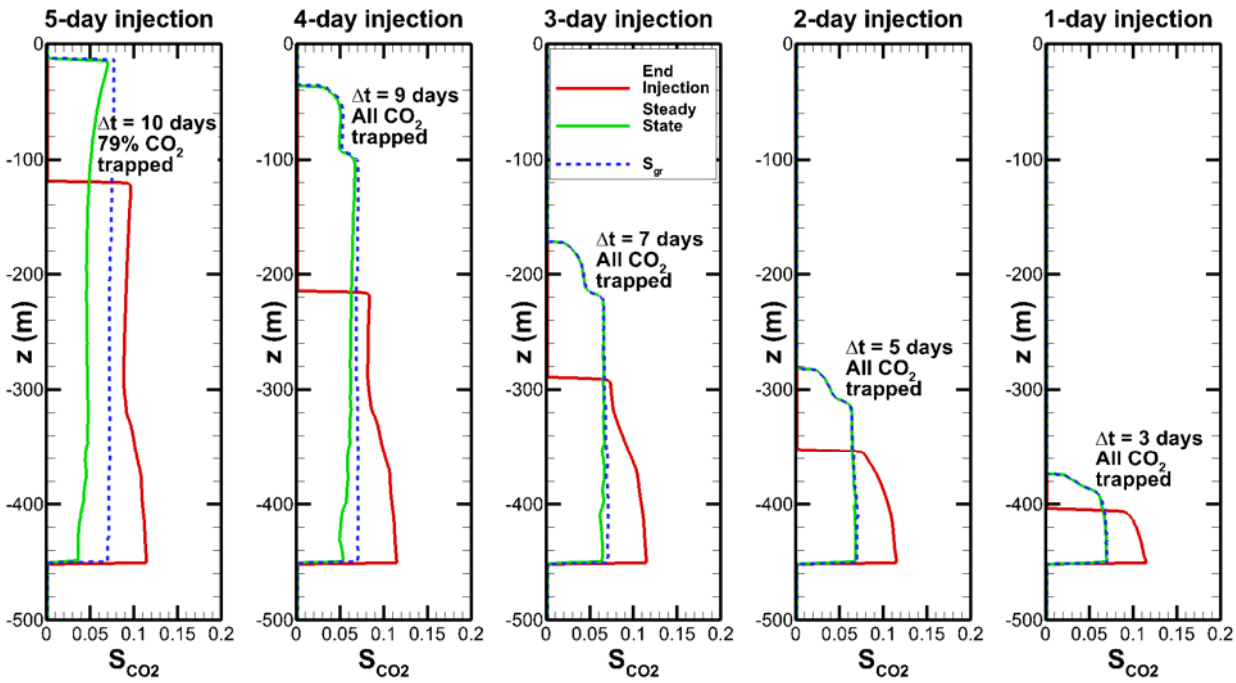

Figure 18. Vertical saturation profiles along the inner radius of the domain at the end of injection and final immobile (trapped) state for different size bubbles. The profile of residual gas saturation S_{gr} is also shown. The variable Δt gives the time between the end of injection and the time steady state is achieved.

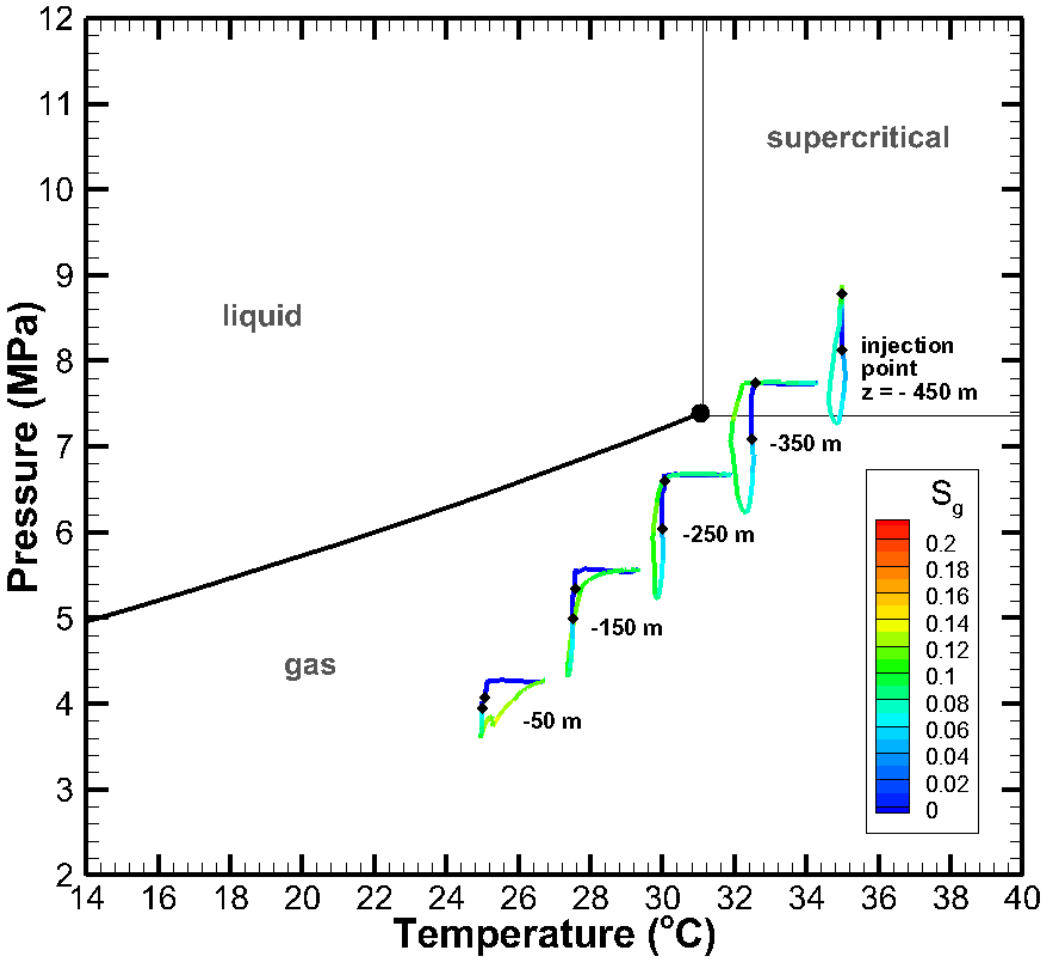

Figure 19. Trajectories over 15 days of *P*, *T*, and CO_2 saturation at five depths for the bubble-rise case with a fixed geothermal gradient boundary condition on the RHS. On each trajectory, the lower black dot shows the initial condition and the upper black dot shows the state at the end of the 5-day injection period.

DISCLAIMER

This document was prepared as an account of work sponsored by the United States Government. While this document is believed to contain correct information, neither the United States Government nor any agency thereof, nor The Regents of the University of California, nor any of their employees, makes any warranty, express or implied, or assumes any legal responsibility for the accuracy, completeness, or usefulness of any information, apparatus, product, or process disclosed, or represents that its use would not infringe privately owned rights. Reference herein to any specific commercial product, process, or service by its trade name, trademark, manufacturer, or otherwise, does not necessarily constitute or imply its endorsement, recommendation, or favoring by the United States Government or any agency thereof, or The Regents of the University of California. The views and opinions of authors expressed herein do not necessarily state or reflect those of the United States Government or any agency thereof or The Regents of the University of California.

Ernest Orlando Lawrence Berkeley National Laboratory is an equal opportunity employer.